IEEE Access
Multidisciplinary | Rapid Review | Open Access Journal

Received 26 August 2022, accepted 2 October 2022, date of publication 26 October 2022, date of current version 7 November 2022.

Digital Object Identifier 10.1109/ACCESS.2022.3217650

RESEARCH ARTICLE

Power Distribution and Propulsion System for an All-Electric Short-Range Commuter Aircraft—A Case Study

JANINE EBERSBERGER[1,2], (Graduate Student Member, IEEE), LEON FAUTH[1,2], (Graduate Student Member, IEEE), RALF KEUTER[1,2], (Graduate Student Member, IEEE), YONGTAO CAO[1,2], (Graduate Student Member, IEEE), YANNIK FREUND[1,3], RICHARD HANKE-RAUSCHENBACH[1,3], BERND PONICK[1,2], AXEL MERTENS[1,2], (Senior Member, IEEE), AND JENS FRIEBE[1,2], (Senior Member, IEEE)

[1]Cluster of Excellence SE[2]A—Sustainable and Energy-Efficient Aviation, Technische Universität Braunschweig, 38106 Braunschweig, Germany
[2]Institute for Drive Systems and Power Electronics, Leibniz Universität Hannover, 30167 Hannover, Germany
[3]Institute of Electric Power Systems—Section for Electric Energy Storage Systems, Leibniz Universität Hannover, 30167 Hannover, Germany

Corresponding author: Leon Fauth (leon.fauth@ial.uni-hannover.de)

This work was supported by the Deutsche Forschungsgemeinschaft (DFG, German Research Foundation) under Germany's Excellence Strategy—EXC 2163/1—Sustainable and Energy Efficient Aviation under Project 390881007, and by the Open Access Publication Funds of the Leibniz Universität Hannover.

ABSTRACT To participate in the transition towards a sustainable use of energy, the aircraft sector needs to be transformed with respect to the energy carrier and propulsion methods. For smaller aircraft, a battery-electric approach is promising. While this will require extensive research and design together with the application of advanced components which are partly not available to this date, general design rules and key parameters and critical components can already be deduced. This publication presents the example design of the full propulsion system for a small commuter aircraft. This serves as a case study to highlight the influence of components and parameters on the overall efficiency and weight of the system. By that, future research can be directed towards the areas of high impact on the realization of all-electric aircraft. A optimization of several motor variants, inverter topologies and power supply grid parameters is performed. The weight of the fully electric propulsion system is dominated by the battery. Therefore, all subsequent components need to be designed towards a high efficiency in opposition to high power density.

INDEX TERMS Aviation, aerospace electronics, AEA, aircraft propulsion, DC/DC converters, electric power supply systems, high voltage direct current, power semiconductor devices, reliability, safety, wide-bandgap semiconductors, wiring harness.

NOMENCLATURE

α	Steinmetz coefficient
β	Steinmetz coefficient
δ	length of air gap
η	efficiency
Γ	area product of inductor
γ	climb/descent gradient
γ'	circumferential angle
$\hat{B}_\mathrm{p}$	flux density fundamental spatial harmonic
$\hat{H}_\mathrm{n}$	normal field strength
$\hat{H}_\mathrm{t}$	tangential field strength
λ	failure rate
μ'	harmonic order of spatial harmonics
μ_0	permeability constant
ω	angular frequency
ϕ	phase angle
$\cos(\varphi)$	power factor
φ	phase displacement

The associate editor coordinating the review of this manuscript and approving it for publication was Chuan Li.

ϑ	temperature
ξ	winding factor
A	electric loading
a	number of parallel windings
A_{core}	core cross-sectional area of inductor
A_{w}	winding window of inductor
B	magnetic flux density
d	duty cycle
D_{i}	inner stator diameter
e_{g}	gravimetric energy density
F	thrust
f	frequency
f_{sw}	switching frequency
g	gravity of Earth
H	magnetic field strength
h	heat transfer coefficient
I	current
I_{123}	phase current
J	current density
k	Steinmetz coefficient
k_{cu}	copper filling factor
L/D	lift-to-drag ratio
l_{Fe}	motor active part length
M	modulation index
m	mass
N	number of turns of inductor
n	rotational speed
P	power
p	number of pole pairs
p_{g}	gravimetric power density
q	slots per pole and phase
S	apparent power
T	torque
U	voltage
U_{123}	phase voltage
U_{DC}	DC-link voltage
U_{dss}	rated voltage
U_{l}	line-to-line voltage
v	speed
w_{sp}	number of turns per coil

ACRONYMS

AEA	All-Electric Aircraft
ANPC	Active Neutral Point Clamped
CPM	Conventional Phase Shift Modulation
DAB	Dual Active Bridge
EASA	European Union Aviation Safety Agency
ECS	Environmental Control System
FAA	Federal Aviation Administration
GaN	Gallium Nitride
HVDC	High Voltage DC
ICAO	International Civil Aviation Organisation
IGSE	Improved Generalized Steinmetz Equation
L/D	Lift-to-Drag Ratio
MOSFETs	Metal Oxide Field-Effect Transistors
MTOW	Maximum Take-Off Weight
NPC	Neutral Point Clamped
OEI	One Engine Inoperative
pax	Passengers
PMSM	Permanent Magnet Synchronous Machine
RBD	Reliability Block Diagram
RCD	Residual Current Device
RMS	Root Mean Square
SiC	Silicon Carbide
SSC	Second Segment Climb
SOC	State of Charge
SSCB	Solid State Circuit Breaker
SPOF	Single Point of Failure
WBG	Wide-bandgap
WIPS	Wing Ice Protection System
ZVS	Zero Voltage Switching

I. INTRODUCTION

The air transport sector currently relies entirely on fossil fuels for propulsion. Two main factors will govern the transition to propulsion methods based on renewable energy. First, the CO_2 emissions need to be reduced. Currently, the transportation sector alone generates 25 % of the global emissions. While road transport dominates this contingent with roughly 75 % of the emissions from the transport sector in comparison to 10 % from air transport, the strong trend towards the electrification of cars will steadily increase the share of the aircraft sector and ultimately demand similar efforts [1]. Additionally, the price of jet fuels will increase sharply due to regulations and the current political situation [2]. Several options exist, and these can ultimately coexist for different applications based on their respective characteristics. Battery electric propulsion can be used for general aviation, small commuter aircraft and short-range passenger aircraft. For larger aircraft, series hybrid approaches, fuel cells or e-fuels can be feasible [3]. In all cases, a high power and energy density of the full propulsion system from energy source to thrust generation is necessary, as additional weight compared to conventional solutions will reduce the carrying capability of persons or cargo. Also, fossil fuels have a high energy density [4], setting a benchmark for future all-electric aircraft. While ultimate solutions and definite numbers can only be determined through extensive design processes, general dependencies and design rules must first be found. Because of the high number of components and parameters, those with the greatest effect need to be focused, to invest the design time according to the possible gain.

Various previous works have focused on the system concept of All-Electric Aircraft (AEA), including safety considerations [3], [5], and on the general feasibility of the full electric approach, showing that it is most viable for short-range commuter aircraft or smaller planes [6], [7]. For larger short-range passenger aircraft like the De Havilland Canada Dash 8, which can seat up to 90 Passengers (pax), it already poses a much greater challenge to achieve a full electric concept that provides a feasible mission range [8]. While other works focus on the design and optimization of

individual components like the electric motor or the converter [9], [10], [11], the work of Barnes [12] already aims to optimize overall electric efficiency of the propulsion system, including battery, converters and motor, but in a lower power class and with motor and inverter models not suitable for application for the requirements of high efficiency and power density propulsion systems for commuter aircraft. Furthermore, Vratny et al. [13] have shown how system voltage affects the efficiency of an electric propulsion system, but only at specific operating points. Also, not only system efficiency but also system weight and safety considerations that may require oversizing of components are important for the overall aircraft performance.

The goal of this publication is to give an overview of the technology scope, and to perform an exemplary design of an all-electric commuter aircraft. By that, the influence of different components and parameters on system efficiency, weight and reliability can give hints for future design processes and research. As a reference model, the Beechcraft King Air 200 is chosen as a widely known and well proven reference. This aircraft gives room for two pilots and 7 - 9 pax depending on the configuration, has a Maximum Take-Off Weight (MTOW) of 5670 kg and a total propulsion power of roughly 1200 kW. To enable the fully electric operation with feasible effort, the aircraft will be used for short-distance commutes (''island hopper'') with a maximum ground distance of 314 km and a cruise speed of 550 km h^{-1} [14]. The general specifications are shown in Table 1. First, the mission profile for the application will be calculated and the supply grid structure and all relevant components will be described. Based on this, simplified assumptions about the propeller are made to enable the design of the electric motor. Three different designs are presented, ranging from high power density to high efficiency. Using these, the inverter generating the three-phase voltage for the electric motor is discussed. Feasible topologies are described and compared in terms of efficiency and power density. Also, DC/DC converters for adapting the supply grid voltage and providing galvanic isolation are evaluated. Next, the wiring harness is considered, including challenges arising from a high voltage design. An overview of battery technology and the limitations in aircraft applications is then provided. After all components have been introduced, critical failure modes and safety considerations are discussed and the reliability of different supply grid structures is calculated. To show general dependencies and the influence of component and parameter variations, different combinations of motor design variants, propulsion system inverter topologies and battery technologies are calculated and compared with respect to overall weight. Based on the results, general design hints can be given.

II. MISSION PROFILE

The maximum ground distance of roughly 314 km is chosen as a representative case for short-range commuter aircraft [15]. Based on the Beechcraft King Air 200 reference aircraft, which offers good short-field capability and climb performance due to its powerful engines, a takeoff power of 1200 kW is chosen for the mission, to enable operations from short, remote airfields [14].

TABLE 1. General specifications of the reference aircraft Beechcraft King Air 200 [14].

Parameter	Value
MTOW	5670 kg
Maximum Airspeed	535 km h^{-1}
Maximum capacity	2 pilots + 9 pax
Propulsion power	2 turboprop engines with 630 kW each
Wing span	16.6 m
Length	13.4 m
Height	4.5 m

TABLE 2. Aircraft performance assumptions.

Segment	Airspeed km h^{-1}	L/D
Takeoff	250	15
Climb	350	23
Cruise	550	19
Descent	550	19
Approach	250	10

The flight mission is composed of a 1-minute takeoff segment, climb to 5000 m, cruise, descent to 1000 m and approach. Additionally, between the descent and approach segment, a reserve mission of about 100 km length consisting of a reserve climb, reserve cruise at 2000 m and reserve descent is added to account for a possible diversion to another airfield. To calculate the performance and power demands of the different flight phases, assumptions are made concerning the airspeed v and the Lift-to-Drag Ratio (L/D) of the aircraft, based on data from similar aircraft and accounting for takeoff and approach configurations [15], [16]. The assumed values are shown in Table 2.

Required thrust F and motor output power P at the propeller shaft can be determined as follows [17]:

$$F = m \cdot g \cdot \left(\frac{1}{L/D} + \sin(\gamma) \right) \tag{1}$$

$$P = \frac{F \cdot v}{\eta_{\text{prop}}} \tag{2}$$

With an assumed constant propeller efficiency of $\eta_{\text{prop}} = 85\%$, which is a conservative state-of-the-art estimation [18], and an aircraft mass of 5650 kg, the required power for cruise flight is 524 kW. By solving the equations shown above for the climb angle γ, the climb and descent rates for the takeoff, climb and descent segments can be calculated assuming a power setting of 1200 kW at takeoff, 1000 kW for the climb segment and 0 kW for the descent. The power requirement of 235 kW for the approach segment is the result of a standard 3° approach path. The complete mission profile is shown in Fig. 1.

III. ELECTRICAL POWER DISTRIBUTION

Based on the requirements already mentioned, a supply grid structure will be designed. This includes the energy storage,

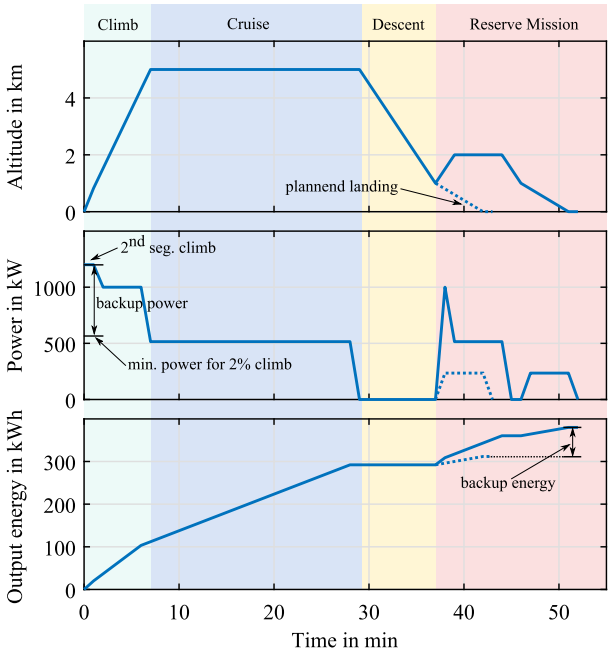

FIGURE 1. Mission profile showing the altitude, total propulsion power demand and output energy demand over the flight time. The propulsion power demand is the total motor output power at the propeller shaft. The output energy demand is resulting from the integration of the output power over the flight time. For sizing the energy storage, the overall efficiency needs to be considered.

wiring harness, safety switches, power electronics converter, electrical motors, and other electrical loads.

A. POWER DEMAND

The main power demand comes from the propulsion system with a peak motor output power demand of 1200 kW at the propeller shafts. To increase the reliability and reduce the overhead for safety reasons, four propulsion units consisting of an inverter, electric motor and propeller are implemented. The system shall be able to deliver the required power even if one of the propulsion units fails, to avoid dangerous situations in case of failures during the take-off or climb. Based on the Federal Aviation Administration (FAA) airworthiness standard for normal category airplanes, §23.21220, a climb gradient of 2% is required with One Engine Inoperative (OEI) at Second Segment Climb (SSC) [19]. Based on equations 1 and 2, this results in a minimum required power of 523 kW. While the situation is less critical for four-engined-aircraft, the additional rotary torque due to unbalanced thrust during OEI needs to be counteracted by applying the rudder, which leads to certain aerodynamic losses of the propulsion power. Even in this situation, the planned peak propulsion power of 1200 kW is completely sufficient to satisfy the requirements. All of the four propulsion units are thus designed for a peak power of 300 kW.

B. ENERGY DEMAND

For a first estimation, only the output energy, meaning the integration of the output power over the flight time as shown in Fig. 1, is considered. If a mostly constant efficiency during the flight mission is assumed, this calculation is sufficient to make assumptions on the backup energy requirement. For sizing the energy storage, the total efficiency needs to be considered as will be shown in the later chapters. The output energy requirement based on the shown mission profile is 311 kW h for the normal mission. If the landing needs to be balked or the destination airport is not available, a reserve mission is planned for, as shown in Fig. 1. This leads to a total output energy requirement of 380 kW h. Energy is provided by four battery packs distributed in the aircraft wings equivalent to conventional fuel tanks integrated in the wings. If, for example one battery fails after 20 min of flight, an output energy of 223 kW h has already been used as shown in Fig. 1, leaving 118 kW h available in the remaining battery packs. To complete the normal mission, an output energy of roughly 88 kW h is necessary, leaving enough margin. Also, a return to the starting airport would be possible. This shows that, by considering the reserve mission when sizing the energy storage, enough margin is already included to allow for the failure of one energy storage unit.

C. GRID STRUCTURE

A wiring harness connects the battery packs with the propulsion units. Because of the high power demand, a high voltage is beneficial to reduce the current and will be discussed in the following chapters. For the grid structure, a number of variants is possible. Each variant is based on the same building blocks, but varies in the interconnection scheme. Every building block is composed of an energy source, a DC/DC converter, the wiring, a three-phase inverter for supplying the electric motor, and the motor itself. Also, a number of safety switches is planned for. In case of a failure in the DC/DC converter, the connection between battery and converter needs to be opened, to prevent a short circuit of the battery. Additionally to the switch at the input of the converter, an additional switch is planned for at the output, to prevent a short circuit of the supply grid in case of a failure in the converter. At the input of the inverter, a switch is needed again to protect the supply grid in case of a failure in the inverter of the electric motor.

A selection of grid structure variants is shown in Table 3 and will be introduced in the following. For the ‘‘fully interconnected’’ variant, the two propulsion units and two batteries per wing are connected to a common DC bus, which enables power transfer between the units. Also, the two sides can be connected by a switch, in case power needs to be transferred to the other side. DC/DC converters are used to regulate the distribution voltage level. This variant requires a large number of safety switches, as each component can be disconnected in case of a failure; also, because of the interconnection of the wings, long cable lengths are required. As an advantage, this variant shows good performance after a single component failure. For example, if one battery fails during the climb segment, the safety switch in the middle can be closed. The remaining power (75%) can be evenly distributed to all four propulsion units, and there is no penalty

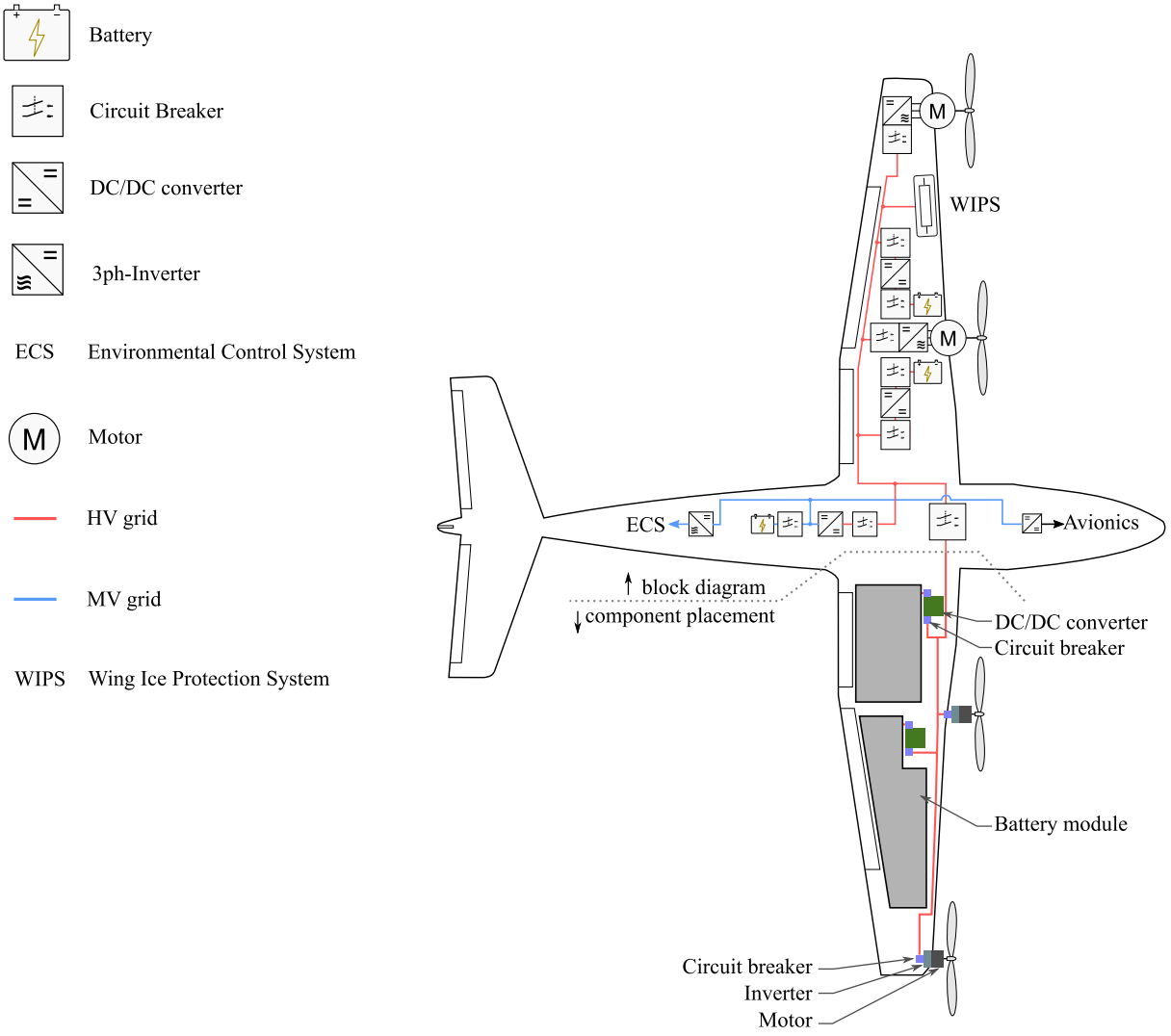

FIGURE 2. Sketch of the power supply system in the "fully interconnected" configuration according to Table 3. Also, an exemplary placement of the components inside the aircraft is shown.

for torque balancing. If one propulsion unit fails, the other three can remain operational, as the faulty unit can be disconnected using a safety switch. However, especially if one of the outer units fails, a penalty due to torque balancing must be expected. The remaining normalized propulsion power is therefore $p < 0.75$. If a battery fails during cruise, again the full remaining energy of the three remaining battery modules (75%) can be utilized without penalty. After one propulsion unit fails during cruise, the full energy of all battery modules remains available. If, for example, the outer propulsion unit fails on one side, the corresponding system on the other side can also be switched off during the cruise phase, as the power demand can be handled by two engines. Thus, no balancing torque is necessary.

The other variants can be analyzed in a similar way. If, for example, no interconnection between the two sides is desired, a cross-connection between the units can be beneficial in terms of post-failure performance, but requires long cable lengths. The worst post-fault performance is reached with the "single" configuration, with four independent strings consisting of energy storage and propulsion unit. As soon as one of the components fails, the complete string has to be switched off. This would result in the lowest remaining available power and energy compared to the other variants. As an advantage, the overall cabling length is short, and the system is also less complex when considering fault handling.

All variants show adequate performance after a single fault in the configuration presented here. Generally speaking, the "single" variant can be used if the propulsion units and batteries are overrated for the absolute minimum safety requirements, as in this case. All other variants are beneficial for a tighter design of the components. Because it has the weight overall, the "fully interconnected" variant is chosen for the design in this publication as a worst-case example.

Fig. 2 shows the system architecture of the electrical power distribution in the aircraft, including the components

discussed earlier in the "fully interconnected" version. Also, the locations of the propulsion units and battery modules are shown. The Wing Ice Protection System (WIPS) located in the leading edge of the wings is directly fed from the high voltage bus for the propulsion system. The Environmental Control System (ECS) and the avionics are supplied by an additional smaller energy storage unit. Additional redundancy is achieved by providing a low-power DC/DC converter to be able to supply the low-voltage components from the high-voltage supply grid. As the power demand from this auxiliary equipment and therefore their weight is much lower than the propulsion power, they will be excluded from the calculations in the following.

IV. PROPELLER & ELECTRIC MOTOR

The propeller and electric Motor are share the same interface of torque T and speed n. To avoid additional frictional losses and mass due to a gearbox, a direct drive is a good solution with high efficiency and power density. The power

$$P = 2\pi \cdot T \cdot n \tag{3}$$

can be realized using various combinations of rotational speed n and torque T. This combination is defined by the propeller and its aerodynamic characteristics, and mainly depends on the most efficient way to convert the required thrust F into torque and speed with the given size and geometry of the propeller blades. Without information about a suitable propeller and the torque-speed relationship, a reasonable motor design cannot be proposed since the torque has in general a bigger impact on the weight of an electric motor than the speed.

A. PROPELLER

In addition to the torque-speed relationship, the installation space is also relevant for the motor design. The installation space can be derived from the hub-to-tip ratio. A typical value for this ratio is 0.15 [18]. Therefore the installation space

$$D_{\mathrm{a,Motor}} = 0.15 \cdot D_{\mathrm{Prop}} \tag{4}$$

is defined in advance. Future work will investigate the variation of the hub-to-tip ratio to determine out the optimum at the interface between motor and propeller.

To gain insight into the interrelationships of propellers, data from certified propellers were collected (Fig. 3). The certification data sheets are provided by the European Union Aviation Safety Agency (EASA) [20]. The speed, torque, diameter and weight were derived at a propeller power $P_{\mathrm{prop}} = 340\,\mathrm{kW}$, as shown in Fig. 3. The results for the current application are shown in Table 4.

The propeller equations combined with the flight mission shown in Fig. 1 result in the data shown in Fig. 4, which provides the foundation for the sizing of the electric motor and the calculation of the overall energy consumption. The altitude and therefore the density of air was considered too, in a simplified way. Equations from [21] were used.

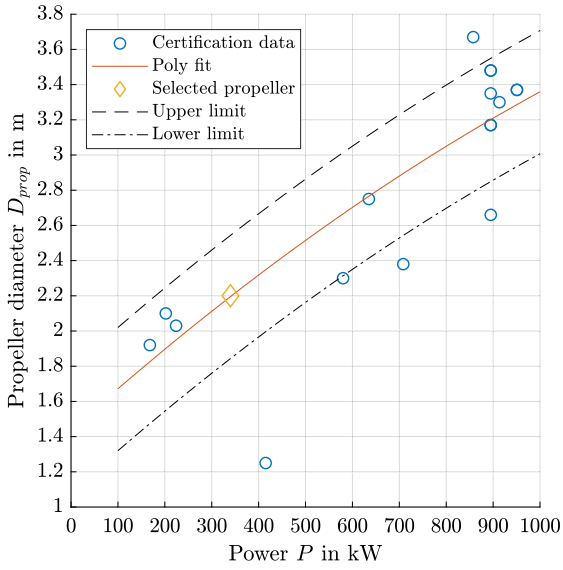

FIGURE 3. Power-diameter relationships of propellers.

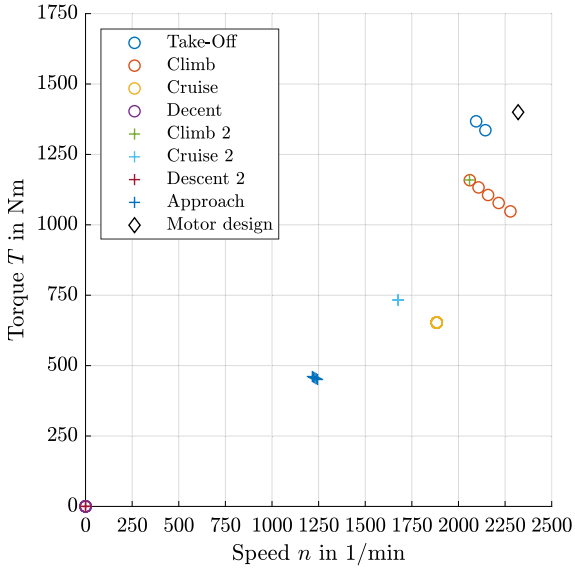

FIGURE 4. Torque-speed operation points of used flight mission and propeller.

B. ELECTRIC MOTOR FOR AIRCRAFT PROPULSION

The motor type is chosen to to be a Permanent Magnet Synchronous Machine (PMSM) due to its high efficiency compared to other motor topologies [22]. The stator is made from cobalt-iron sheets to allow for high flux densities up to $B = 2.3$ T. The winding system is a tooth-coil winding with cooling channels to allow high current densities and so achieve high power density based on the investigations. The rotor is set up as a spoke-magnet type rotor. The benefits are high air-gap flux densities and the absence of a yoke. Additionally, the magnets are protected against demagnetization as they are embedded in the rotor. The magnets are NdFeB type magnets with a remanence flux density of $B_{\mathrm{r}} = 1.3$ T. The

TABLE 3. Overview of supply grid structures.

	Fully interconnected	Dual connected	Cross connected	Single
Diagram	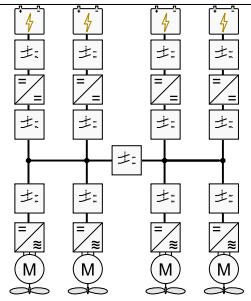	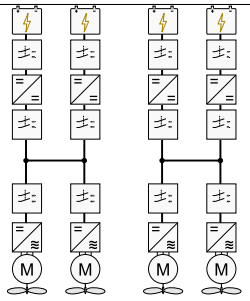	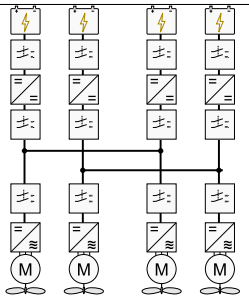	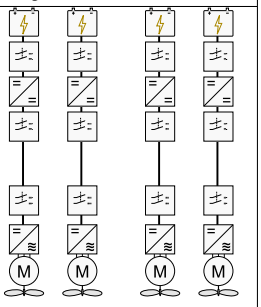
Number of safety switches	13	12	12	12
Cable length	21.7 m	11.4 m	23.0 m	8.0 m
Post-fault performance	++	0	+	-

outer diameter is set by the propeller and its hub diameter. The inner diameter should be scaled up as far as it is beneficial. A disadvantageous increase in the inner diameter occurs when the cross-section of the conductor is reduced too much and the torque decreases due to reduced current. Therefore, several iteration steps needed to be performed. The equation for the torque

$$T = \pi \mu_0 \cdot l_{Fe} \cdot \left(\frac{D_\mathrm{i}}{2}\right)^2 \cdot \hat{H}_\mathrm{t} \cdot \hat{H}_\mathrm{n}. \tag{5}$$

shows that the inner diameter has a strong impact on the torque. With a large inner diameter, a greater number of pole pairs is beneficial to reduce the size of the yoke. To realize a large number of pole pairs a tooth-coil winding is beneficial. The fractional-slot concentrated winding adds the advantage of a short end winding. This reduces the joule losses and improves the efficiency. Additionally, it is easier to implement a direct conductor cooling from a manufacturing perspective compared to a distributed winding.

The winding scheme can be varied in terms of the number of parallel strands a and the number of turns per coil w_sp, since field weakening is not necessary. Limitations arise only from the conductor geometry in terms of the ratio of width to height. Therefore optimization with regard to the voltage can be performed without affecting the motor characteristics, provided that no unfavorable conductor geometries are needed. At a very low number of turns per coil, strong current displacement effects take place. With a very high number of turns per coil, the conductor becomes very thin and the overall insulation percentage increases to an unfavorable degree (low copper filling factor k_cu). The variation of the number of parallel strands a and the number of turns per coil w_sp can be done without affecting the motor characteristics, so long as the electrical load

$$A(\gamma', t) = -\sum_{\mu'} \sqrt{2}\xi_{\mu'} \cdot \frac{m\mathrm{w}I_1}{\pi \frac{D_\mathrm{i}}{2}} \sin\left(\mu'\gamma' - \omega t + \varphi\right) \tag{6}$$

TABLE 4. Overview of data concerning the chosen propeller.

Parameter	Value
Power P_prop	340 kW
Speed n	2320 1/min
Torque T	1400 Nm
Diameter D_prop	2.2 m
Weight m_prop	50 kg

about the circumferential angle γ' remains the same. The equation for the terminal voltage is not affected by the motor current I_1. The terminal voltage U_1 can be described approximately by

$$U_1 \approx \frac{\omega}{\sqrt{2}} \cdot (\mathrm{w} \cdot \xi_p) \cdot \frac{2}{\pi} \cdot \frac{\pi \frac{D_\mathrm{i}}{2}}{p} \cdot l_\mathrm{Fe} \cdot \hat{B}_\mathrm{p} \tag{7}$$

neglecting the ohmic resistance and leakage reactance. The maximum flux density of the fundamental spatial harmonic stays constant with a constant product of motor current and number of turns per coil. Therefore, variation of the voltage U_1 causes a change in the motor current I_1. This can be performed in a limited range of the conductor geometry adapted to the number of turns per coil $\mathrm{w_{sp}}$. An example of the employed conductor geometry with $\mathrm{w_{sp}} = 8$ can be seen in Fig. 5. The tool from which the image is taken is also used to generate an estimate of the copper fill factor with realistic heat transfer properties.

To pursue the overall goal of a power train with minimum mass, a useful combination of power density and efficiency of the motor is needed. Whether power density or efficiency has the bigger impact on the overall weight depends on the overall system, the aircraft type and application. This is why different machine categories (M1 to M3) with different characteristics have been designed. Table 5 shows the designs and their differences. The current density J is one of the parameters with the biggest impact on power density and efficiency. The winding material is usually copper, but to achieve the highest power density, aluminum is an option

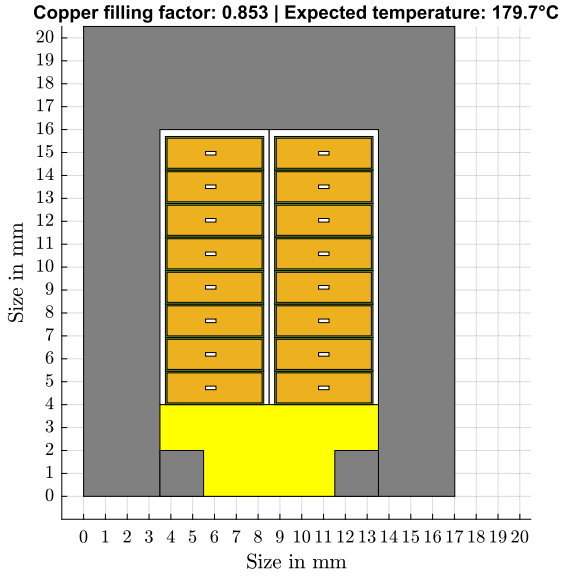

FIGURE 5. Cross-section through a direct-liquid-cooled slot in the motor M1. Grey: Electrical steel sheet, Yellow: GFK wedge, Green: Insulation, Orange: Conductors, White: Insulation film.

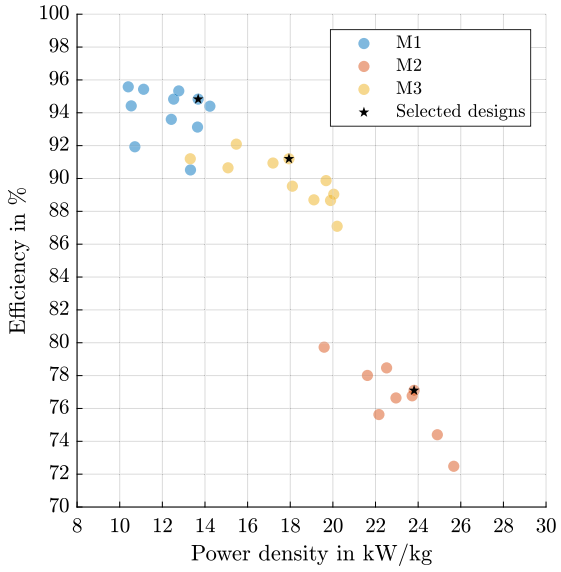

FIGURE 6. Power density and efficiency of electric motor designs used in the parameter study at a peak power of $P = 340$ kW.

TABLE 5. Overview of the motor types and their characteristics.

Motor	Purpose	J in A/mm^2	Winding	m_{mag}
M1	High efficiency	25	copper	high
M2	High power density	75	aluminum	low
M3	Trade-off	50	copper	medium

to consider. The increase in power density due to the lower density of aluminum is a trade off since aluminum has a lower conductivity and therefore increases the joule losses. The amount of magnet mass m_{mag} also determines the shift in direction of higher efficiency (higher magnet mass) or to higher power density (lower magnet mass).

The different designs follow the rules developed in [23]. These include, in particular, the implementation of short tooth tips, thick magnets which are buried, a larger distance between the conductors and the air gap, and a high split ratio (ratio of inner diameter D_{i} to outer diameter D_{a}). A large number of pole pairs is required to allow a large inner diameter and, at the same time, to utilize the cross-section (width of teeth) in terms of high flux densities. For all designs, a pole pair-number of $p = 25$ is chosen. Using the propeller speed, (Table 4) the maximum frequency can be calculated to be $f_1 = 966$ Hz. The air-gap length is set to $\delta = 1$ mm to reduce the magnetic resistance across the air gap without going so far as to make the manufacturing challenging. The fractional-slot concentrated winding intended to achieve a short end winding and a high pole-pair number were chosen with a number of slots per pole and per phase of $q = 2/5$. To find an ideal geometry and a feasible trade-off between power density and efficiency, the parameter yoke height, tooth width and inner diameter were varied. To consider the trade-off between the integration of cooling channels and the reduction of the copper filling factor k_{cu}, an inlet temperature of $\theta_{\text{in}} = 40°C$ and an outlet temperature of $\theta_{\text{in}} = 80°C$ at the maximum allowable winding temperature of $\theta_{\text{w}} \approx 180°C$ were considered. The cooling channel was sized using an iterative loop to achieve the highest possible copper filling factor at the allowable temperature. The models of the motor category M2 needed a higher heat transfer coefficient to achieve comparable copper filling factors. A higher heat transfer coefficient can be achieved with higher coolant velocities, which increase the volumetric flow and pressure drop. This would lead to higher cooling power and therefore mass, but both is not considered. The results can be seen in Fig. 6.

The power density and efficiency from FEA calculations concerning the electric motor categories M1 to M3 were calculated at maximum power requirement using the mass of the active part (stator sheets, winding, magnet, rotor sheets). For a more realistic approach, a rough design for the additional components like the housing, shaft and bearings was carried out for the selected designs shown in Fig. 6. A sketch of a motor which is constructed as mentioned above is shown in Fig. 7. In the vicinity of the end winding, the carbon-fiber tube which hydraulically separates the stator from the rotor and enables the direct liquid cooling of the conductors conductors can be seen. The assumptions concerning the motor construction are shown in Table 6.

The table with the final designs (Table 7) shows three different electric motors with their interfaces to the power train. The efficiency η has an impact on the battery weight and the amount of power which the power electronics needs to provide. The power factor $\cos(\varphi)$ defines the apparent power and therefore influences the necessary size of the power electronics. For the cooling system (pumps, heat exchanger, pipes), the heat transfer coefficient h of the

TABLE 6. Assumptions for the weight correction of the electric motors.

Assumption	Value
Shaft thickness	10 mm
Housing thickness	8 mm
Endplate thickness	8 mm
Bearing DE	2 kg
Bearing NDE	1.75 kg
Separation tube thickness	2 mm

FIGURE 7. Half-section of a sketch of a electric motor with direct-liquid-cooled tooth coils, a spoke magnet type rotor and a hollow shaft.

TABLE 7. Final motor designs considered in the system analysis.

Motor	p_g in kw/kg	η in %	$\cos(\varphi)$	k_{cu}	h in W/m^{2}K
M1	7.97	94.83	0.88	0.85	3500
M2	11.15	75.04	0.53	0.80	20500
M3	9.61	90.90	0.74	0.83	3500

direct-liquid-cooled coils, which is mainly dependent on the coolant velocity, provides a constraint for the design of the components. This step was simplified by using the losses of the electric motor.

Next, safety considerations for PMSMs will be discussed. Among the dominant failure modes of PMSMs, bearing failure accounts for almost fifty percent [24], and is mainly induced by mechanical factors such as poor lubrication, vibration, operational environment and overload [25]. The failure mode of the rotor could also result from the bearing current, if the drive system is designed to use a high voltage and high switching frequency. Winding failure accounts for the second dominant failure mode in electric motors, which is mainly caused by overload or breakdown of the insulation. The insulation of the winding is especially challenging due to the high voltage and low-pressure working conditions of the aircraft during cruise [26]. With the help of a three-level inverter systems instead of a two-level inverter, the lower voltage slew rate not only reduces the stress on the winding insulation, but also reduces the bearing current effect. Also, demagnetization of the permanent magnet could also reduce the performance and create abnormal torque vibration. In order to provide predictive maintenance for PMSMs, aging effects relating to the permanent magnets can be observed using online parameter identification methods.

V. POWER ELECTRONICS

Two types of power electronic system are used in the on-board electrical distribution system. DC/AC inverters supply the motors with a symmetrical three-phase input by converting the power from the High Voltage DC (HVDC) grid. In addition, the transferred power and fundamental frequency can be controlled. DC/DC converters are utilized to connect the battery modules to the HVDC grid and to step up the voltage. The step-up converters provide a stable output voltage independent of the State of Charge (SOC) of the batteries. Furthermore, the output voltage can be chosen virtually independent of the maximum battery module voltage.

In the following subsections, the modeling of the power electronic systems is described. First, suitable semiconductors are selected. Second, the design of the inverters and the converters is presented. Finally, safety considerations concerning the power electronic systems are detailed.

A. POWER SEMICONDUCTORS

Wide-bandgap (WBG) semiconductors will be key enablers in future power electronic systems due to their superior properties, such as low on-state resistance, low switching energies and high thermal conductivity. Compared to silicon-based inverters and converters, the efficiency and power density can be increased [27], [28]. Rising availability and falling costs are expected, so that it will be easy to employ WBG semiconductors in future electric aircraft. As discussed in Section III, HVDC grids will be implemented in electric aircraft. As manufacturers are currently researching 3.3 kV and 6.5 kV Silicon Carbide (SiC) Metal Oxide Field-Effect Transistors (MOSFETs) [29], [30], [31], good commercial availability can be assumed for 2040. Therefore, SiC MOSFETs are to be preferred over Gallium Nitride (GaN) devices, which currently provide rated voltages of only up to 800 V.

In [32], a SiC semiconductor loss model is presented which takes into account the expected rated voltages of the future. This model is used in the inverter and converter design in Sections V-B and V-C, with rated voltages independent of actual manufactured voltage classes. To generate more practice-oriented results, the common manufactured semiconductor voltage classes are used for the system optimization in Section IX, e.g., 650 V, 1.2 kV, 1.7 kV, 3.3 kV, 6.5 kV.

TABLE 8. Line voltage U_l, phase voltage U_{123}, phase current I_{123}, DC-link voltage U_{DC} and modulation index M for various combinations of parallel winding branches a and number of coil turns w_{sp} for M3 with a power factor of $\cos\varphi = 0.7367$.

a	w_{sp}	U_l	U_{123}	I_{123}	U_{DC}	M
2	10	588	340	503	1000	0.9607
2 / 1	12 / 6	706	408	419	1200	0.9607
2 / 1	14 / 7	824	476	359	1400	0.9607
1	8	941	543	314	1600	0.9607
1	9	1059	611	279	1800	0.9607
1	10	1177	679	251	2000	0.9607
1	13	1530	883	193	2500	0.9991
1	15	1765	1019	168	3000	0.9607

Additionally, a voltage class of 2.3 kV which is already available for silicon IGBTs [33] is added, to close the gap. Furthermore, the voltage utilization of the power semiconductors is assumed to be 66 % in the power loss calculation, which considers the over-voltage protection needed because of the parasitic inductance in the electric drive system and the harsh working conditions. Additional significant voltage derating of power semiconductors is not considered necessary in this case, since the flight altitude is lower than that of large passenger aircraft. With the help of the four-motor architecture, the reliability requirement of the inverter system could also be reduced further. For power loss calculation, a quadratic dependence of the switching losses on the rated voltage is assumed [32].

B. INVERTER DESIGN

Beside conventional two-level inverters, three-level inverters such as T-type, Neutral Point Clamped (NPC) and Active Neutral Point Clamped (ANPC) inverters are considered for the propulsion inverters, based on the models described in [32]. For the ANPC inverters, two modulation strategies are examined. The SC-PWM focuses on reducing the conduction losses [34] and the ND-PWM on reducing the switching losses [35]. As described in Section IV-B, different combinations of parallel winding branches a and number of coil turns w_{sp} can be realized to achieve different combinations of voltage and current at the machine terminals, while keeping the output power constant. This can be used to adjust the DC-link voltage for the same electric motor design. As an example, Table 8 shows various combinations for the moderate motor design M3 for DC-link voltages from 1 kV to 3 kV, with the respective modulation index at the design point of the semiconductors. The chip area optimization and weight calculation follow the description in [32]. Furthermore, the models allow for any rated voltage of the semiconductors independent of the actual voltage classes available. The inverter weight includes the weight of the DC-link capacitors, the liquid-cooled heat sink, the semiconductor modules, the housing, the busbar, and the driver boards. DC-link capacitors serve as DC filters by stabilizing the voltage across the inverter terminals. Furthermore, they provide the energy for fast current commutation. Filters on the AC side are omitted,

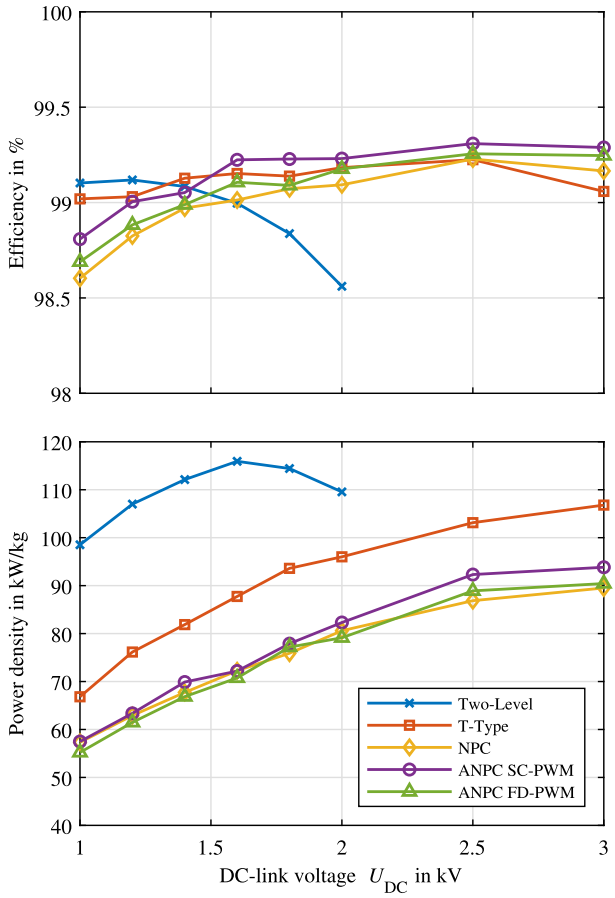

FIGURE 8. Comparison of two- and three-level inverter topologies for motor design M3 with a switching frequency of $f_{sw,Inv} = 30$ kHz at peak power demand during climb ($P_{Inv,out} \approx 380$ kW).

since their additional weight can be avoided by co-optimizing the inverter and motor designs. An integrated design, in which the inverter is placed as close as possible to the motor, can overcome the need for output filters [36], [37]. In addition, by choosing a three-level topology, smaller voltage steps and slopes stress the motor less compared to a two-level topology. For the capacitors, the worst-case operating point with a modulation index of $M \approx 0.61$ and a power factor of $\cos\varphi = 1$ is considered [38].

In order to determine the most suitable topology, the efficiencies and gravimetric power densities of different inverter designs are examined in Fig. 8 with $f_{sw,Inv} = 30$ kHz, which was determined to be a suitable switching frequency in [32]. The semiconductors in two-level inverters have to block the full DC-link voltage, whereas the semiconductors in NPC and ANPC inverters only have to block half of the DC-link voltage. In T-type inverters, both types of semiconductor are required. Due to the quadratic dependence of the switching losses on the rated voltage, this leads to a drastic reduction in the efficiency of the two-level inverter as shown in Fig. 8. However, the two-level inverter achieves the highest gravimetric power density for DC-link voltages up to 2 kV. For higher DC-link voltages, no chip area exists that can

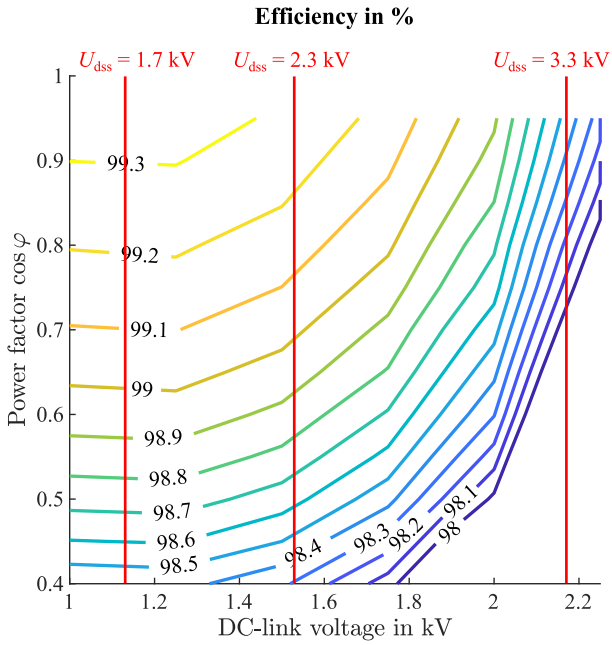

FIGURE 9. Design results for the efficiency of a 2-level inverter with variation of the DC-link voltage and power factor. The calculations are made for a switching frequency of $f_{sw,Inv} = 30$ kHz, a modulation index $M = 1$, and a constant output power $P_{Inv,out} = 500$ kW.

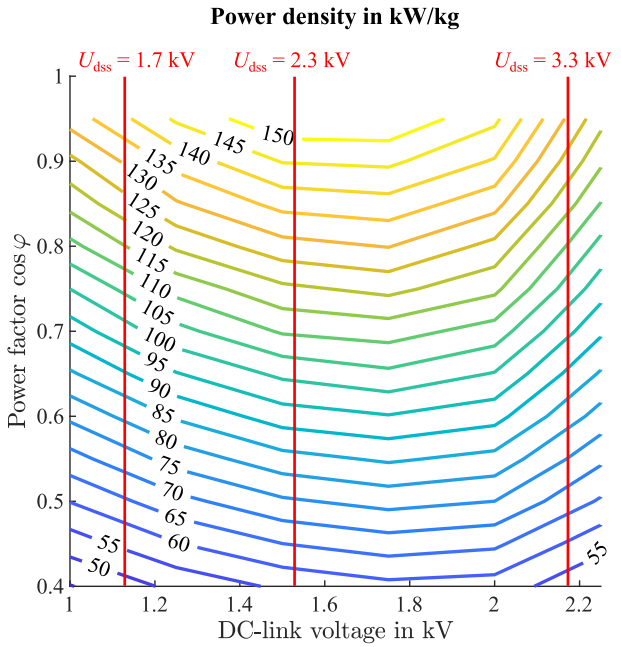

FIGURE 10. Design results for the power density of a 2-level inverter with variation of the DC-link voltage and power factor. The calculations are made for a switching frequency of $f_{sw,Inv} = 30$ kHz, a modulation index $M = 1$, and a constant output power $P_{Inv,out} = 500$ kW.

dissipate the semiconductor losses of the two-level inverter. The T-type inverter has a higher power density than the three-level inverter for the full voltage span, while the ANPC inverter with SC-PWM has the highest efficiency starting from roughly $U_{DC} = 1.5$ kV. The ultimate selection of the topology needs to be determined by a system optimization considering all other components, especially the batteries.

Since the power factor $\cos\varphi$ is an important variable in the motor design, the design results with varying power factors, DC-link voltages, a constant modulation index $M = 1$ and an output power of $P_{Inv,out} = 500$ kW are shown as an example for two-level inverters in Fig. 9 and Fig. 10. A high power factor results in both a high efficiency and high gravimetric power density of the inverter. In addition, the designs with a voltage derating of 66 % for the voltage classes 1.7 kV, 2.3 kV and 3.3 kV are marked. Possible minimum power densities are achievable in a range of DC-link voltages from 1.4 kV to 1.8 kV, as shown in Fig. 10. However, this range is not covered by the expected voltage classes with acceptable voltage utilization. In general, a high power factor of the motor is necessary for a high power density of the inverter. In contrast, a high power density of the motor will lead to a lower power factor and therefore a lower power density of the inverter. Which of the two variants is more beneficial for minimizing the total propulsion system weight, needs to be determined by the global system optimization.

C. CONVERTER DESIGN

For selecting and designing the DC/DC converter, first of all the constraints need to be determined. Due to the minimum voltage demand from the motor as shown in Table 8, it is expected that the supply grid voltage will be equal to or higher than the battery voltage. Therefore, a step-up converter can be applied as the simplest solution. If the required gain of DC/DC converter is above certain limits because of a high selected supply grid voltage, the step-up converter can be of disadvantage due to the uneven distribution of losses in the semiconductors and the general lower efficiency as they generally operate at hard switching [39]. For such operation points, the application of isolated DC/DC converters like for example the Dual Active Bridge (DAB) can be beneficial. The required voltage gain is achieved by the turns ratio of the high frequency transformer, the losses in the semiconductors are evenly distributed, and soft switching is realized, which reduces the losses and the electromagnetic interference. The general complexity of the topology and the required control is higher compared to the simple step-up converter. As an additional advantage, galvanic isolation between the battery module and the supply grid is achieved. This can be beneficial or even required for a number of situations. In case of high supply grid voltages, the grounding of the middle point can be beneficial to reduce the isolation stress. An exemplary 3 kV-grid can thus be realized as ±1.5 kV, which reduces the isolation effort in the wiring by half. Also, the supply grid can be realized as IT network without the need for additional Residual Current Devices (RCDs) for passenger protection.

Due to the benefits described, the DAB is chosen as a suitable topology for the DC/DC converters in an electric aircraft. It consists of a low-voltage and a high-voltage full bridge which are connected by a transformer. The rated

voltages of the semiconductors are chosen for each side based on the maximum battery module voltage, which is assumed to be $U_{\mathrm{Bat,mod}} = 1000\,\mathrm{V}$, and on the DC-link voltage. The DAB is operated with Conventional Phase Shift Modulation (CPM), maximum duty cycles of $d_1 = d_2 = 0.5$ and a phase shift of $\frac{\pi}{2}$ at the design point for maximum power transfer. The calculation of the required leakage inductance of the transformer, its Root Mean Square (RMS) current and the semiconductor conduction losses are based on [40], [41]. By designing the transformer winding ratio (transmission ratio) according to

$$\frac{U_{\mathrm{Bat,mod}}}{U_{\mathrm{DC}}} = \frac{U_1}{U_2} = \frac{N_1}{N_2} = \frac{I_2}{I_1} \tag{8}$$

ideal Zero Voltage Switching (ZVS) of the semiconductors can be assumed. Therefore, only the turn-off losses are taken into account. The respective switching currents are calculated by the expressions given in [42].

A simple core-type shape with one winding on each leg is assumed for the transformer. Following the descriptions in [43], the amorphous alloy 2605SA1 with a saturation flux density of $B_{\mathrm{sat}} = 1.56\,\mathrm{T}$ [44] is chosen as the core material. The geometric dimensions are determined starting with the calculation of the area product

$$\Gamma = \underbrace{\frac{U_1}{4 \cdot f_{\mathrm{sw,DAB}} \cdot N_1 \cdot B_{\mathrm{max}}}}_{A_{\mathrm{core}}} \cdot \underbrace{\frac{2 \cdot I_1 \cdot N_1}{J_{\mathrm{max}} \cdot k_{\mathrm{cu}}}}_{A_{\mathrm{w}}} \tag{9}$$

which results from the multiplication of the core cross-sectional area A_{core} and the winding window A_{w}. It is proportional to the transferred power. Furthermore, a copper filling factor of $k_{\mathrm{cu}} = 0.4$, a maximum current density of $J_{\mathrm{max}} = 4\,\mathrm{A\,mm^{-2}}$, and a maximum flux density of $B_{\mathrm{max}} = 1.3\,\mathrm{T}$ are assumed. For the sake of simplicity, the winding window and the core cross section area should be equal $A_{\mathrm{w}} = A_{\mathrm{core}} = \sqrt{\Gamma}$. Then the total number of turns is determined by the single equation for the core cross-sectional area. The windings are distributed so that a winding window as square as possible is created on each side of the transformer. The winding losses are determined by the RMS current, the specific resistance of copper, the total mean winding length and the winding cross cross-sectional area. The winding cross cross-sectional area, which in turn is calculated using the RMS current and the maximum current density. By using litz wires, the AC losses can be neglected in the frequency range considered. The analysis presented in [43] shows that the core loss calculation using the Improved Generalized Steinmetz Equation (IGSE) leads to the best results and it is therefore applied in this transformer design with the Steinmetz parameters of 2605SA1: $\alpha = 1.51, \beta = 1.74, k = 6.5$.

The dependence of the DC-link voltage and the switching frequency of the DAB on its efficiency and power density is studied in advance to identify beneficial operating points. Fig. 11 shows that an increase in the switching frequency at high DC-link voltages leads to higher efficiency and higher

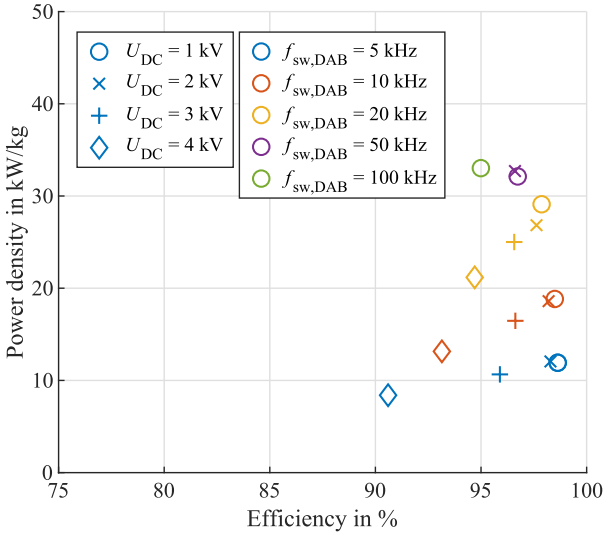

FIGURE 11. Trade-off between power density and efficiency of the DAB depending on the switching frequency $f_{\mathrm{sw,DAB}}$ and the DC-link voltage U_{DC} with a maximum battery module voltage of $U_{\mathrm{Bat,mod}} = 1000$ V and an output power of $P_{\mathrm{DAB,out}} = 500$ kW.

power density. At low DC-link voltages, the efficiency first increases with an increase in switching frequency and then decreases again, e.g., at $f_{\mathrm{sw,DAB}} = 10\,\mathrm{kHz}$ for $U_{\mathrm{DC}} = 2500\,\mathrm{V}$, while the power density consistently increases. At the lowest voltage considered, the efficiency only decreases with increasing switching frequency. The effect can be explained by the decrease in the area product with increasing switching frequency. Therefore, the core cross-sectional area, the number of turns and the winding window all decrease, leading to a smaller total weight and core volume. On the one hand, the core losses decrease with a decrease in core volume. On the other hand, they grow with increasing switching frequency, since all types of core loss rise with frequency. Additionally, the semiconductor switching losses increase with switching frequency. Because of that, for a switching frequency higher than $f_{\mathrm{sw,DAB}} = 20\,\mathrm{kHz}$, only low DC voltages can be realized as otherwise the losses in the semiconductors are too high. This can be seen in Fig. 11: While the peak efficiency over all DC voltage levels is largely unchanged below $f_{\mathrm{sw,DAB}} = 20\,\mathrm{kHz}$, for higher frequencies the efficiency decreases, while the increase in power density is getting smaller.

Since these trends in regard of the voltage level stand in contrast to the behavior of the other components such as the inverter (see Section V-B) and the wiring harness (see Section VI), a complete system analysis is required.

D. SAFETY CONSIDERATIONS FOR POWER ELECTRONIC SYSTEM

For high power and high voltage aircraft power conversion systems, SiC MOSFETs are considered to be among the most promising power semiconductors due to their high efficiency and high breakdown voltage capability. However, the failure rate of the power semiconductors could increase

dramatically because of the applied high blocking voltage and increased exposure to cosmic radiation experienced in aircraft applications at high altitude. By adopting three-level inverters instead of two-level inverters, the voltage stress on each power semiconductor can be reduced to half for the same DC-link voltage, which could potentially reduce the failure rate induced by cosmic radiation, allowing a higher voltage utilization. Due to the lower reliability requirement compared to large aircraft and lower flight altitude in this case study, 66 % of voltage utilization by the power semiconductors is chosen, this is comparable to the typical voltage utilization of power semiconductors in high voltage inverter systems for electric vehicle. Furthermore, hermetic sealing technology and mission-profile-oriented thermal management should be implemented, since moisture-related failure could be induced by the changing environmental temperature during the flight mission. Compared to power semiconductors based on silicon, SiC MOSFETs using the latest technology show worse power-cycling capability [45]. Maintenance strategies based on the mission profile and thermal stress analysis are recommended. Other specific failure mechanisms of SiC MOSFETs, such as the breakdown of gate oxide and bipolar degradation [46], are being investigated by researchers. they are expected to be improved in commercial products in the coming years.

The domain failure modes and mechanisms of DC-link capacitors in power electronic systems vary among the capacitor types employed. Generally, the applied voltage and the hot-spot temperature are the two common critical stress factors for capacitors. Apart from these two stress factors, moisture corrosion induced by the temperature changes along the flight mission could also be one of the most critical factors affecting the reliability of film capacitors. Mandatory hermetic sealing and mission-profile-oriented thermal management could extend the lifetime of film capacitors. For large aluminum electrolytic capacitors, the lifetime is also limited by the increase of leakage current, resulting from the eltrochemical reaction of oxide layer. Other main factors causing the failure of ceramic capacitors include insulation degradation and flex cracking [47].

The reliability of power electronic systems can be further improved if fault-tolerant operation strategies can be utilized. For example, three-level ANPC or dual inverters can still provide full performance or reduced performance under several fault scenarios when adequate fault-tolerant operation strategies are implemented [48]. This kind of fault tolerance is especially helpful if a critical failure occurs during the take-off phase, when maximal power is required.

VI. WIRING HARNESS

The wiring harness is used to transfer the energy from the batteries to the motor inverters. It therefore needs to be dimensioned for peak propulsion power demand divided by the efficiencies of the motor and inverter. As this leads to high power an increased voltage is proposed to reduce the current and consequently the overall weight of the wiring harness. To design the wiring harness, both the current-carrying conductor and the insulation need to be considered.

Generally speaking, transmission of direct current at high voltages can be the preferred solution for this application when compared to alternating current, as additional AC losses like the skin effect and the impedance of the cable capacitance do not arise. Also, as the energy source provides direct current, fewer inverters and rectifiers are needed compared to AC transmission. However, the design of safety switches and fuses is more complex for DC transmission, because an electric arc is not extinguished by the zero crossing of the voltage, as it is in AC systems. As an alternative to high voltage distribution, superconducting power transfer should be discussed. While this would simplify the challenges concerning the insulation of high voltages, superconductivity is not preferred for this application, as it requires considerable auxiliary equipment and also special approaches to interconnections. Especially the interface between a superconducting transmission line and any connected equipment at ambient temperatures, like power electronic converters, needs to be evaluated. While the operation of power electronics at cryogenic temperatures has already been investigated [49], the complexities and costs cannot be justified for this application. An example cross-section of a cable for conducting high voltage direct current is shown in Fig. 12. It consists of an inner stranded conductor for flexibility, a conductor shield, an insulation, insulation shield and additional taping or armouring on the outside, to protect the insulation. The requirements on the cable are defined by the current-carrying capability and the insulation of the high voltage. In terms of conductor material, a decision between high electrical conductivity on the one hand and specific weight on the other hand needs to be made. While aluminum conductors offer a reduced weight compared to copper, their conductivity is lower. Also, to date, aluminum conductors are not approved for certain aircraft applications [50]. One phenomenon observed in wiring harnesses for aviation is so-called arc tracking. This means that an electric arc forms between two conductors when organic insulation is degraded or damaged [51]. The minimum required voltage for starting arc tracking is reduced with lower pressure, as happens in aircraft applications [52]. Therefore, this effect is less severe for lower cruise altitudes as in this example, but should be considered nevertheless during the design of the cabling. The effect typically occurs with polymer-based insulation which is contaminated by condensation or dust. As a consequence, hydrophobic materials offer an advantage in preventing arc tracking. It could be shown that by adding nano fillers, which increase the hydrophobicity of the insulation, the danger of arc tracking can be reduced [53]. The damage to the conductor is dependent on the conductor material [54] and can be more severe for aluminum conductors. As an alternative, special composite conductors consisting of an aluminum core with a copper cladding can be used, combining the advantages of copper and aluminum [55]. Especially the thermal short-circuit strength is comparable to that of copper.

Historically, insulation of cabling in aircraft applications was provided by polyimide tape (KAPTON®) [56], polytetrafluoroethylene (TEFLON®), ethylene tetrafluoroethylene (TEFZEL®) and laminates or combinations of the aforementioned materials [57]. The current material of choice for the highest requirements is cross-linked ethylene tetrafluoroethylene (XL-ETFE) because of its moisture resistance, mechanical stability, flame retardance and light weight. Compared to the standard ETFE material, a higher thermal stability is gained by cross-linking, giving a rated temperature of 200 °C [58]. Such materials are promising for future applications in AEA. The use of cross-linked polyethylene (XLPE), which is used in HVDC transmission cables, has also been suggested, but as its rated temperature is usually below 150 °C, its application in aircraft cabling is not feasible.

The calculation of various parameters of the cabling in dependence on the chosen DC-link voltage is shown in Fig. 13. As this depends heavily on the chosen materials and safety factors, this can only serve as an illustrative example. For a fixed power, the current and therefore the required copper cross-section are reduced with higher voltage, while the insulation thickness is increased. This can lead to a certain optimum point at which the overall weight of the cabling is minimized; in this case, the optimum occurs at around 3 kV. The losses in the cabling are generally reduced with higher voltages, but above a certain voltage, the decline is less pronounced. Lastly, the temperature difference across the insulation needs to be calculated. This is dependent on the losses in the cable, the thickness of the insulation and its thermal conductivity. If the temperature difference is too high, the aging of the material can be accelerated. Also, effects like arc tracking, as mentioned before, become more likely. For the example supply grid structure shown in Fig. 2, a total cabling length of roughly 22 m is necessary. Considering an example voltage of 3 kV, this would lead to an overall cabling weight of 17 kg and losses of 1.58 kW during peak power requirements at climb for the positive and negative voltage rails combined. As many other devices in the supply grid are also heavily dependent on the selection of the voltage, a reasonable choice can only be made by a global optimization (see Section IX).

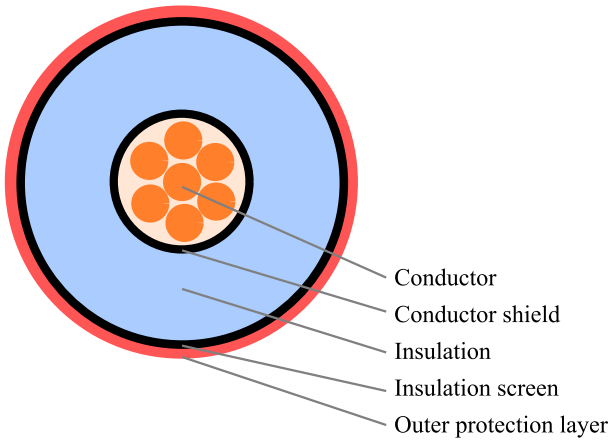

FIGURE 12. Example cable cross-section.

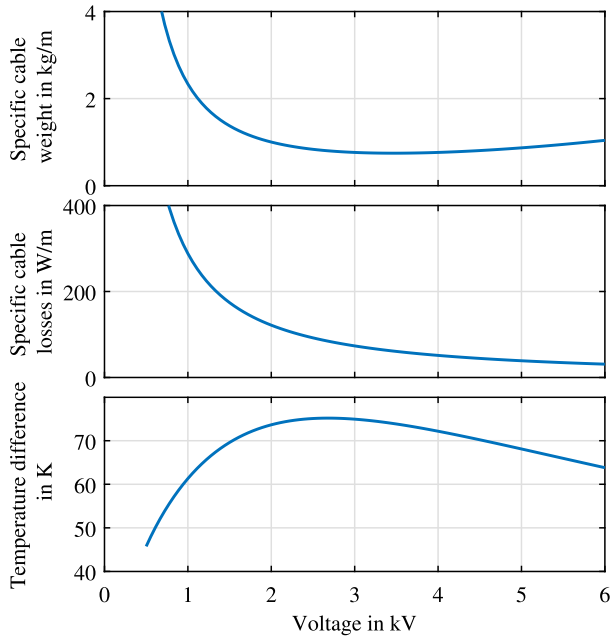

FIGURE 13. Calculation of various parameters of the wiring harness in dependence on the voltage when considering both the positive and negative voltage rails. For the calculation, a conductor made from a copper-aluminum-laminate and a XL-ETFE insulation was considered.

VII. BATTERIES

When choosing the energy storage for fully electric aircraft for this application, batteries are the most feasible solution. Fuel cell systems can be evaluated as an alternative, but require special spherical or cylindrical tanks to store either pressurized or cryogenic hydrogen, making their integration into the aircraft more difficult, whereas batteries allow for a greater freedom of design because the available space in the wings can be well utilized by adapting the shape of the battery modules. Currently, lithium-ion (Li-ion) batteries give the highest energy density in general, but for demanding applications like aviation, more parameters need to be considered. Based on the individual mission profile, a stronger focus needs to be put on either the energy density or the power density. Also, for smaller aircraft sizes, it is not only the typically quoted gravimetric density which is important, but also the volumetric density. When designing the overall electrical grid, the battery system voltage is an important parameter.

Currently available energy storage systems based on Li-ion batteries, both for residential storage and traction applications, can only reach energy densities in the region of 160 $\mathrm{W\,h\,kg^{-1}}$ and 160 $\mathrm{W\,h\,L^{-1}}$ [59] and power densities up to 800 $\mathrm{W\,kg^{-1}}$ and 800 $\mathrm{W\,L^{-1}}$. This includes the packaging as well as the balancing system. For systems which can be employed in aviation, much higher performance is required, and this is difficult to achieve with common Li-ion batteries using graphite for the negative electrodes, due to

the low specific capacity of graphite. For future developments, a gravimetric energy density of 500 W h kg^{-1} is aimed for [60], which can most likely be achieved with lithium-metal batteries. Subtypes of lithium-metal batteries are the lithium-sulfur (Li-S) and the lithium-air (Li-Air) chemistries.

Currently, lithium-metal chemistries are only capable of very few charge and discharge cycles, making them unsuitable for practical applications [61]. Lithium-sulfur batteries can offer an alternative to Li-ion batteries because of their potentially lower cost. Energy densities comparable to Li-ion batteries can be achieved if certain technical challenges can be overcome [62]. Also, as stated earlier, not only the gravimetric, but also the volumetric energy density is of great importance in this application. While the gravimetric energy density of Li-S batteries is promising, to match the volumetric energy density of Li-ion, the compositions of the cathode and anode materials have to be chosen carefully. In this way, a gravimetric energy density of 700 W h kg^{-1} and a volumetric energy density of 1000 W h L^{-1} can be achieved [63]. It should be noted that these numbers refer to the performance on a cell level. For the full battery module, this value must be substantially reduced. An example of a realized design is shown in [64]. By producing pouch-type cells, a gravimetric energy density of up to 400 W h kg^{-1} could be demonstrated, but the number of discharge cycles is still low (< 100). In terms of the reliability of Li-S batteries, the road towards their commercialization is mainly limited by the self-discharge problem and short cycle life [65], with the shuttle phenomenon potentially causing degradation of the individual cells [66]. A health monitoring system is therefore necessary to predict the battery lifetime and develop the corresponding maintenance strategies. Furthermore, efforts need to be made to prevent the lithium-sulfur battery from exploding, since its organic electrolytes have a low flash point and the carbon-sulfur composite materials are prone to explode. Several intrinsic approaches used to reduce the fire risk associated with lithium-sulfur batteries on the cell level are summarized in [67]. On the battery module level, mission-profile-oriented battery thermal management is required to prevent the battery from overheating. The implementation of fire control strategies is also mandatory to meet the certification requirements, which include fire detection devices, extinguishing agents and isolated fire zones for distributed energy storage systems to prevent a fire from spreading [68].

Li-air batteries are a concept still under research. The most promising functional prototype shows a gravimetric energy density of 500 W h kg^{-1} and can be charged and discharged 100 times [69].

Special environmental conditions experienced by batteries in aviation are the large ambient temperature swing, the low air pressure, and cosmic radiation. For typical flight missions, ambient temperatures ranging from $-70\,^{\circ}$C at high altitude up to $50\,^{\circ}$C at airports in hot regions must be expected. Generally speaking, lower temperatures reduce the usable capacity of the battery, while higher temperatures can lead to a shorter lifetime overall [70]. This results in the need to control the battery temperature. Most critical is take-off from airports in hot locations, because of the additional heating of the battery cells due to the high power demand. This can even lead to thermal runaway, where the excessive heat energy cannot be removed fast enough, leading to a constant build up of heat. This can result in outgassing of the battery cells, producing gas which can pose a health hazard, and ignition of the battery pack [71]. As a result, thermal management of the battery pack is mandatory, increasing the lifetime and reducing the risk of thermal runaway [72]. Especially the active cooling during take-off and climb can result in a high additional energy demand. During flight at high altitude, waste heat from the propulsion system could be used to heat the batteries if necessary. While a reduced air pressure generally will have no effect on the normal operation of the battery, it can influence the behaviour during thermal runaway. It was found that a reduced air pressure can reduce the heat release of Li-ion batteries during thermal runaway, making this failure more containable, but, in the same time, the risk due to toxic or flammable gases was increased [73]. While an influence of radiation on the battery concept could be demonstrated [74], this was only evident for space applications, where much higher radiation doses occur. For aviation applications, no effect of radiation on the batteries is expected.

From the mission profile shown in Fig. 1, a minimum output energy demand of 380 kW h and a peak power of 1200 kW are determined, resulting in a peak discharge rate of $C = 3.15$. Based on the redundancy concept detailed further in Section VIII, an overrating in terms of battery power and energy is already included in these numbers. For illustration, a mass of 1300 kg is reserved for the energy storage in the initial guess. This number is further supported by the system optimization in section IX. Based on this number, a gravimetric energy density higher than 250 W h kg^{-1} and a gravimetric power density higher than 1000 W kg^{-1} would be required. This shows that these values, and therefore the feasible battery technology, are strongly dependent on the application. In this particular example, the power density is of more importance than the energy density, making even the application of Li-ion batteries feasible; these show a higher maturity and are therefore more likely to be approved by the safety agencies compared to Li-metal chemistries. A more detailed optimization of the battery parameters is presented in Section IX.

While Li-ion battery packs with battery module voltages of around 400 V have been commonly used in electric vehicles of recent years, there are developments that aim to increase the battery module voltage to 800 V or even 1000 V. Although this development in the automotive sector is mainly driven by the attempt to increase charging power for electric vehicles, it can also help to reduce the overall system weight [75]. A high battery voltage can be beneficial to allow for fast charging to minimize downtime. Also, if the gain between battery voltage and supply grid voltage is small, simple DC/DC converter topologies like step-up converter can be

used, reducing the complexity. For utilizing the individual battery cells as much as possible, an intelligent battery management system is necessary, which is more challenging to realize for higher battery voltages. This also ultimately limits the maximum feasible battery voltage level. If a low battery voltage of for example 400 V is combined with a isolated DC/DC converter like a DAB, the semiconductors on the primary side can be selected from a lower voltage class, which can result in a higher efficiency. Considering the recent developments in this field, a maximum battery module voltage of 1000 V is assumed to be feasible for the time frame considered.

VIII. SAFETY CONSIDERATIONS ON THE SYSTEM LEVEL

System reliability can be improved by using more reliable components and an optimized system architecture. Several reliability improvement methods on the component level were introduced in the last several sections. In this section, important safety considerations on the system level will be discussed.

A. DESIGN CONSIDERATIONS FOR SYSTEM ARCHITECTURE

A simplified system architecture is one of the guiding principles when aming to improve the system reliability and maintainability. In this case, the low voltage supply system will be directly supplied from a separate distributed low-voltage battery rather than from the high-voltage DC bus through a step-down converter.

The reliability of the system can be further improved by striving for fault-tolerant design. By adopting a four-motor fault-tolerant architecture with distributed battery modules, not only can the overall reliability be greatly improved compared to a twin-motor architecture, but the system can also be less oversized [5].

The fault-tolerant architecture is based on necessary protective devices. With the help of DC circuit breakers, faulty components can be isolated and the system reconfigured. The circuit breakers in this application are mainly positioned between the battery and DC bus as well as between DC bus and propulsion inverter (see Fig. 1). For example, in order to make full use of the energy source to extend the flight range when a fault occurs in the drive system, the faulty component needs to be isolated using a circuit breaker. A second DC circuit breaker can then connect the two high-voltage DC buses in a fully interconnected structure (see 3), although these are isolated in normal operation. Especially safety switches for high power aircraft applications are not available yet and need to be evaluated by future research.

Solid State Circuit Breaker (SSCB) are beneficial in terms of weight, but offer no galvanic isolation. Mechanical switches, however, have a low power density. The most promising are so-called hybrid circuit breakers, which are a combination of solid-state switches for arc-free switching and mechanical switches for providing galvanic isolation [76]. Compared to passive/active resonance DC circuit breakers, hybrid circuit breaker offer faster response times and a reduced risk of arcing [77]. A hybrid circuit breaker with galvanic separation and fail-safe functionality is especially suitable for use between two high voltage DC buses to avoid Single Point of Failure (SPOF). The isolation of the faulty component can also be combined with the break-less approaches, such as deactivation of the inverter systems in case of motor failure.

First-generation products already exist for industrial applications [78]. Typical requirements can be fulfilled, like a minimum of 10,000 switching events for extended maintenance intervals and at least three breaking operations under fault condition, according to [79]. Currently, these devices are only specified for altitudes up to 2000 m, so for application in aircraft, the reduced air pressure needs to be considered. If galvanic isolation is provided by an air gap in a mechanical switch, the distance needs to be increased accordingly. At an altitude of 5 km, the breakdown field strength of air is reduced to 18 kV cm^{-1} compared to 25 kV cm^{-1} at 2 km [80], according to the Paschen Law. Based on this, a voltage derating of at least 0.7 should be planned. Also, for all safety switches incorporating power semiconductors, like SSCB and hybrid circuit breaker, cosmic radiation needs to be considered. As stated already, voltage derating is necessary, and this should be at least 0.85 for 5 km altitude. Based on the switch topology and application, the dominant derating mechanism can be chosen.

The hybrid circuit breaker from [78] can achieve a gravimetric power density of 400 kW kg^{-1}, if the derating is considered. Currently available circuit breakers with aircraft approval only reach power densities of 20 kW kg^{-1} [81], showing that the application of SSCBs or hybrid switches is absolutely necessary to meet the weight requirements. The practical application of these circuit breakers depends on approval for aircraft use by the regulating agencies. If no fuel is used in the aircraft, clearance for use in explosive environments is not necessary, simplifying the housing of the breaker. Based on the currently available products, the availability of hybrid circuit breakers with aircraft approval and the power density mentioned above is feasible in the estimated time frame.

For overcurrent handling, additional fuses should also be planned. Currently available high-power DC fuses can reach power densities of 300 kW kg^{-1} when considering a voltage derating because of the reduced air pressure. [82]. Practical application is again dependent on approval by the safety agencies. The currently realized power density is high enough to neglect the weight of the fuses compared to, for example, the battery module.

In order to protect crew and passengers from leakage current, RCDs are mandatory in aircraft designs. A ''type B'' RCD, which is able to detect a leakage current with DC components, is recommended for DC grids in [77]. For future applications, advanced RCD solutions with a real-time leakage current monitoring function are expected for electric aircraft system architectures [83].

TABLE 9. Target allowable failure probability per flight hour at different risk levels based on the aircraft type [85].

Certification level	Probable	Remote	Extremely Remote	Extremely Improbable
0-6 pax, SRE	$< 10^{-3}$	$< 10^{-4}$	$< 10^{-5}$	$< 10^{-6}$
0-6 pax, STE, ME	$< 10^{-3}$	$< 10^{-5}$	$< 10^{-6}$	$< 10^{-7}$
7-9 pax	$< 10^{-3}$	$< 10^{-5}$	$< 10^{-7}$	$< 10^{-8}$
10-19 pax	$< 10^{-3}$	$< 10^{-5}$	$< 10^{-7}$	$< 10^{-9}$

SRE: Single Reciprocating Engine, STE: Single Turbine Engine
ME: Multi-Engine

B. CONSIDERATION OF MAIN CERTIFICATION REQUIREMENT

The safety considerations for small aircraft (up to 19 pax) follow the certification specifications 23 (CS-23) and the related guideline Advisory Circular (AC), which are regulated by the FAA. Different countries may have their own safety-related regulations or guidlines, however, these are generally all oriented towards the requirements of the International Civil Aviation Organisation (ICAO). Since small aircraft (up to 19 pax) are less complex than large passager aircraft, lower failure probability values for catastrophic failure conditions are required [84]. The target allowable average probabilities per flight hour at different risk levels and for different aircraft types are listed in Table 9. For example, the average catastrophic failure probability of the aircraft in this case (7 - 9 pax) should be lower than 10^{-8}/h. Quantitative system reliability is usually analysed using a Reliability Block Diagram (RBD), in which the reliability models of the subsystems are connected in series or parallel. If a constant failure rate λ is assumed for a component, its reliability function $R(t)$ can be represented by an exponential distribution: $R(t) = e^{-\lambda t}$. The overall system reliability and the average failure probability per flight hour can then be calculated based on basic probabilistic and statistical theory [86]. Since the overall system in this case is designed for 2040, the failure rates of the components based on current knowledge naturally involve great uncertainty, especially concerning the not-yet-mature new battery system. In order to quantitatively compare the system reliabilities for different system architectures, several assumptions are made:

1) Only the propulsion system is considered in the system reliability analysis.
2) The failure rates of the components in the propulsion system are assumed to remain constant throughout the useful life according to the bathtub curve theory; the reliability of the drive system will be reset after each flight, since systems with constant failure rate have no 'memory'.
3) The failure rates of the components are based on the study in [87] (see Table 10). As stated before, the reliability prediction for the battery has not been studied thoroughly and is with great uncertainty, the reliability data for the battery system the Pipistrel Alpha Electro is used as reference [87] for the comparative study. The failure rate of the DC/DC converter is considered to be comparable with that of the inverter.
4) The system shall be considered failed when only 3/4 of the total power is available (without considering the effect of torque balance due to asymmetric thrust).
5) The failure rates of other components with much higher orders of reliability, such as cables or protection devices, can be neglected in the analysis.

TABLE 10. Failure rates of the components in the propulsion systems [87].

Component	Failure rate λ
Battery stack	$4.95 \cdot 10^{-6}/h$
DC/DC converter	$3 \cdot 10^{-6}/h$
Inverter	$3.81 \cdot 10^{-6}/h$
PMSM	$5.93 \cdot 10^{-6}/h$
Propeller	$1 \cdot 10^{-7}/h$

TABLE 11. Selected critical failures of the main electric components in the electrified aircraft propulsion systems.

Components	Selected critical failures
PMSM	Bearing degradation (electrical and mechanical) Breakdown of winding insulation Permanent magnet degradation
SiC MOSFET	Single event burnout Thermal mechanical stress induced degradation Humidity induced degradation Gate oxide breakdown Bipolar degradation
DC link Capacitor	General: thermal and electrical over stress Film capacitor: humidity induced degradation Aluminium capacitor: electrochemical reaction Ceramic capacitor: insulation degradation and cracking
Wiring	Arching Partial discharge Surface charges
Li-Ion battery	Electrical overstress (overcharge, external short circuit) Mechanical damage (crush or penetration) Thermal overstress Capacity degradation

Several critical failures of the main electric components in the electric propulsion systems are summarized in Table 11.

A simplified RBD of the fully interconnected architecture is shown as an example in Fig. 14. The result in Fig. 15 shows the failure probabilities of different system architectures for this case study. As can be seen from the figure, the fully interconnected system architecture has the lowest failure probability. The system reliabilities of the dual-connected architecture and cross-connected architecture are equal under the given definition of system failure (Assumption 5). However, the flight performance of the aircraft with the cross-connected system architecture is better than that of the dual-connected system architecture under the single-device failure scenario, due to the less asymmetric thrust. Among all the system architectures, the single-grid structure has the worst system reliability due to less hot redundant components.

For all architectures, the failure probability after one full flight mission of approximately 50 min is less than $2 \cdot 10^{-9}$, which is below the requirement of $1 \cdot 10^{-8}$ as given in Table 9.

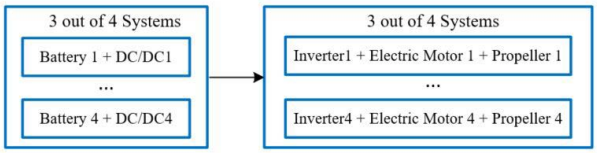

FIGURE 14. Simplified reliability block diagram of the electric aircraft drive system.

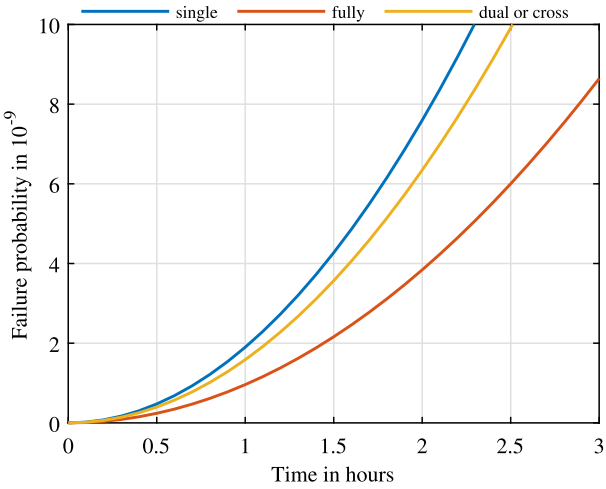

FIGURE 15. Failure probabilities of different aircraft system architectures.

Therefore, the reliability of the designed system is sufficient. It has to be noted, that the application of the same system for longer flight missions can be critical, as shown in Fig. 15. This shows additional demand for research in reliability of the subsystems, fail-safe components and redundancy concepts.

C. OTHER SPECIFIC SAFETY CONSIDERATIONS

Lightning strike is a common danger for airplanes. The increasing electrification of aircraft can increase the risk of serious failures resulting from a lightning strike and therefore needs to be considered during the design of the supply grid. In conventional aircraft of older design, the fuselage and wings were built from metal, creating an inherent conductive enclosure and protecting the internal electrical equipment. In this way, the aircraft body itself conducts the current during a lightning strike, and the sensitive electrical components are mostly spared from damage. In future designs with composite material bodies made from, for example, carbon fibre, which has a low conductivity, additional protection measures are important. These include metal meshes or foils and wiring nets integrated into the body material, which are connected to a defined ground plane like the engine housing. This creates a highly conductive path for the lightning current, especially close to locations with a high probability of lightning strike, like the radome, wing tips and propulsion units. As an additional measure, all sensitive components and wiring sections need to be equipped with overvoltage protection. This can take the form of varistors or spark gaps [88].

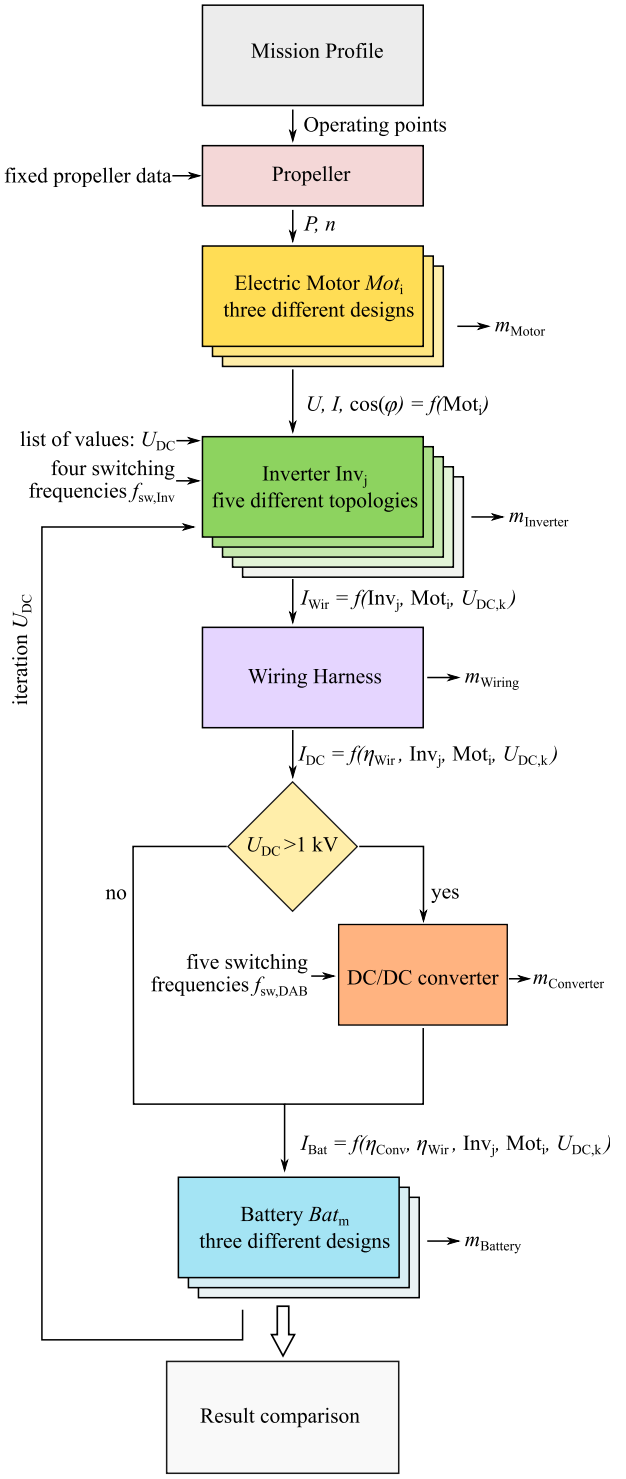

FIGURE 16. Methodology for system optimization.

IX. SYSTEM OPTIMIZATION

To find the best system design with the lowest overall weight while fulfilling all safety requirements, the individual components are evaluated together according to the design flow diagram in Fig. 16. The mission profile introduced in Section II provides the input for the propeller design, which

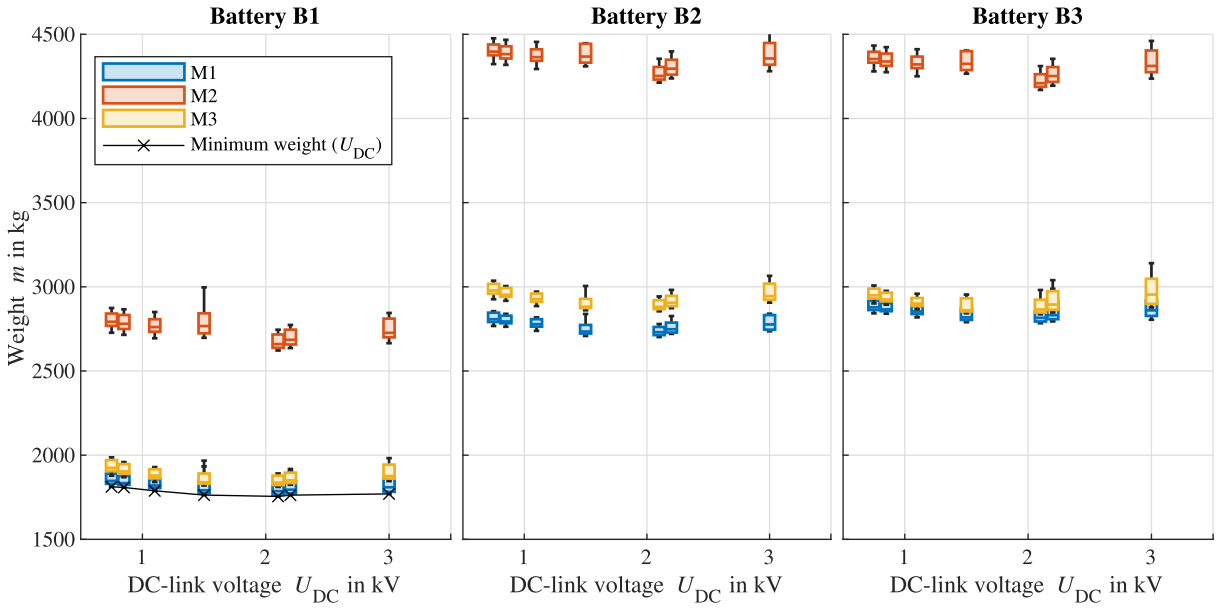

FIGURE 17. Comparison of the final design configurations: each plot shows the overall weight for the full propulsion system for one battery type. B1: high-power Li-ion battery; B2: High-energy Li-S battery; B3: State-of-the-art automotive traction battery. The different motor designs are denoted by color. The boxes contain various combinations of inverter topologies, inverter and converter switching frequencies. The outliers are excluded from the plot (outlier = values more than 1.5 · IQR (interquartile range) away from the box). The weight of the propellers is excluded.

results in the torque and speed requirements for the electric motor. Three motor variants are presented in Section IV-B. The design focuses on a variant with high power density, a variant with high efficiency and a variant consisting of a compromise between the two. The information about the required current, voltage and power factor is used for the inverter design, including four switching frequencies and four different topologies as described in Section V-B. The required current of the inverters is fed into the calculation of the wiring harness, according to Section VI, and based on the "fully interconnected" grid structure detailed in Section III. The DC/DC converter is designed using the required power of the HVDC grid and considering five switching frequencies - see Section V-C. For the batteries, three different combinations of power and energy density and a mean battery discharge efficiency of 98 % are assumed. A maximum battery module voltage of 1 kV is assumed, for higher voltages a DC/DC converter needs to be applied. In summary, the following parameters are varied in the study:

1) Motor design:
   a) M1 (high efficiency),
   b) M2 (high power density),
   c) M3 (trade-off)
2) Supply grid voltages:
   $U_{DC} \in$ [750 V, 850 V, 1100 V, 1500 V, 2100 V, 2200 V, 3000 V, 4000 V]
3) Inverter topologies:
   a) Two-level,
   b) Three-level T-type,
   c) Three-level NPC,
   d) Three-level ANPC with SC-PWM and ND-PWM
4) Inverter switching frequencies:
   $f_{sw,Inv} \in$ [10 kHz, 30 kHz, 50 kHz, 70 kHz]
5) Converter switching frequencies:
   $f_{sw,DAB} \in$ [1 kHz, 5 kHz, 10 kHz, 15 kHz, 20 kHz]
6) Batteries:
   a) B1: high-power Li-ion design, optimistic assumption:
      $e_{g,1} = 300\,\mathrm{Wh\,kg^{-1}}$, $p_{g,1} = 1200\,\mathrm{W\,kg^{-1}}$
   b) B2: high-energy Li-S design ([63]):
      $e_{g,2} = 700\,\mathrm{Wh\,kg^{-1}}$, $p_{g,2} = 700\,\mathrm{W\,kg^{-1}}$;
   c) B3: State-of-the-art automotive battery, 2020 Tesla Model 3 long-range performance:
      $e_{g,3} = 171\,\mathrm{Wh\,kg^{-1}}$, $p_{g,3} = 708\,\mathrm{W\,kg^{-1}}$

TABLE 12. Ten best results with battery B1 and motor M1.

#	Inverter topology	DC-link voltage	$f_{sw,Inv}$	$f_{sw,DAB}$	Weight[1]
1	Two-level	2100 V	10 kHz	20 kHz	1755 kg
2	ANPC SC-PWM	2100 V	30 kHz	20 kHz	1756 kg
3	T-type	2100 V	10 kHz	20 kHz	1757 kg
4	T-type	2100 V	30 kHz	20 kHz	1757 kg
5	ANPC ND-PWM	2100 V	30 kHz	20 kHz	1758 kg
6	ANPC SC-PWM	2100 V	50 kHz	20 kHz	1758 kg
7	ANPC ND-PWM	2100 V	50 kHz	20 kHz	1758 kg
8	ANPC SC-PWM	2100 V	10 kHz	20 kHz	1758 kg
9	NPC	2100 V	30 kHz	20 kHz	1759 kg
10	ANPC ND-PWM	2100 V	10 kHz	20 kHz	1760 kg

For the required power of the entire drive train, the design point with the maximum power demand is evaluated. The recooling dissipates the losses of the drive train and is accounted for with a constant power-losses-to-weight ratio of 10.4 $\mathrm{kW\,kg^{-1}}$ is assumed [89]. For the required energy

[1]The weight of the propellers is excluded.

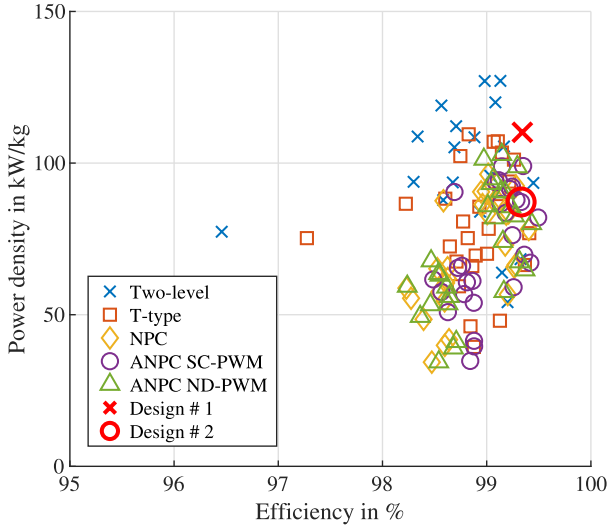

FIGURE 18. Optimization results for the inverter for different switching frequencies, topologies, and DC-link voltage levels. Motor M1 and battery B1. Fixed converter switching frequency of $f_{sw,DAB} = 20$ *kHz*. Trade-off between power density and efficiency at nominal power. Best designs are highlighted.

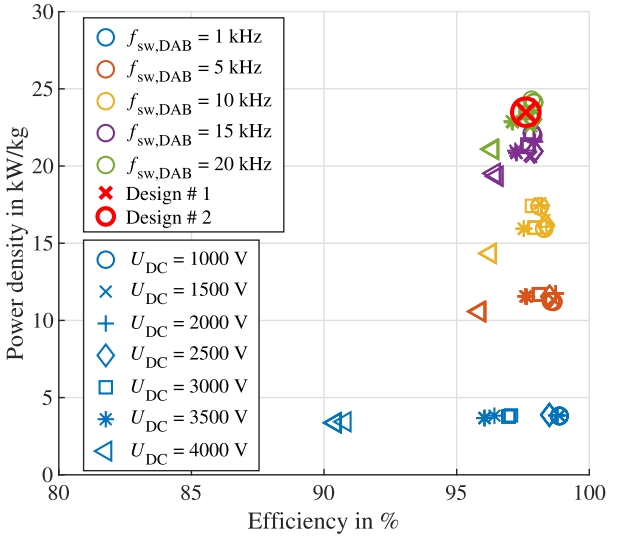

FIGURE 19. Optimization results for the DAB converter for different switching frequencies and DC-link voltage levels. Motor M1 and battery B1. Fixed inverter switching frequency of $f_{sw,Inv} = 30$ kHz. Trade-off between power density and efficiency at nominal power. Best designs are highlighted.

of the battery modules, the mission profile shown in Fig. 21 is considered. Consequently, the complete flight mission is calculated for all relevant components.

The results of the weight calculation are shown in Fig. 17. Clearly, battery B1 with the highest power density and motor M1 with the highest efficiency lead to the lowest total weight. Due to the relatively short mission duration and the relatively high total installed power in this case study, the power density requirement for the battery is more important than the required energy density. In addition, the curve showing the dependence of the minimum weight on the DC-link voltage is marked indicating the lowest weight at $U_{DC} = 2100$ V. Within the ten best results, the total weight hardly changes ($\approx$ 5 kg) while the switching frequency of the converter is $f_{sw,DAB} = 20$ kHz and only the inverter topology and its switching frequency are varied; see Table 12. Particularly beneficial are inverter switching frequencies from 10 kHz to 50 kHz and the ANPC and T-type inverters. However, the lowest weight of 1755 kg is achieved with the two-level inverter. Since the total weight is relatively insensitive to the inverter design, different criteria such as potentials for post-fault performance can form the focus of the optimization. Therefore, the ANPC with SC-PWM and $f_{sw,Inv} = 30$ kHz is selected for the final design.

A comparison of the efficiency and power density of the inverter and converter for battery B1 and motor M1 is shown in Fig. 18 and 19, in which the designs # 1 and # 2 are highlighted. From the results, it can be concluded that for the inverter design, efficiency is the more important criterion, while for the converter, its power density is of greater importance. However, it should not be inferred that the other objective can be neglected. This conclusion depends strongly on the gradient of the Pareto front, e.g., a higher converter efficiency costs much more in power density.

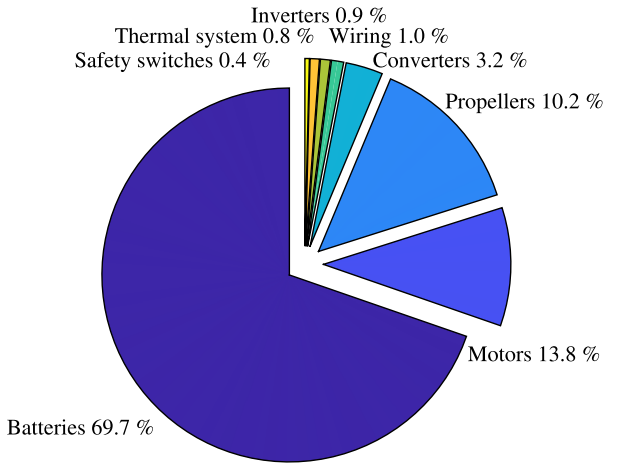

FIGURE 20. Weight distribution of the final design # 2 with a total of 1956 kg: battery B1, motor M1, DC-link voltage $U_{DC} = 2100$ V, ANPC inverter with SC-PWM and a switching frequency of $f_{sw,Inv} = 30$ kHz, converter switching frequency $f_{sw,DAB} = 20$ kHz.

The weight distribution of the final design is shown in Fig. 20 and illustrates the importance of battery technology research, as the batteries account for $\approx$ 70 % of the total weight. The motors are the second largest contributor at $\approx$ 14 %. The weights of the other components have a minor impact on the overall weight. Thus, their efficiency is particularly important for reducing the total weight by reducing the weight of the batteries.

The mission profile of the final design is shown in Fig. 21. It illustrates the propeller speed n, motor output power $p_{Motor,out}$, motor apparent input power $s_{Motor,in}$, motor line voltage u_l, motor phase current i_{123}, motor power factor $\cos\varphi$, and the efficiencies of the motor, converter, inverter, wiring and whole system. Both the inverter and converter perform at high efficiencies of $\approx 98\,\% - 99\,\%$. The wiring is almost lossless. The motor M1 achieves a very high power

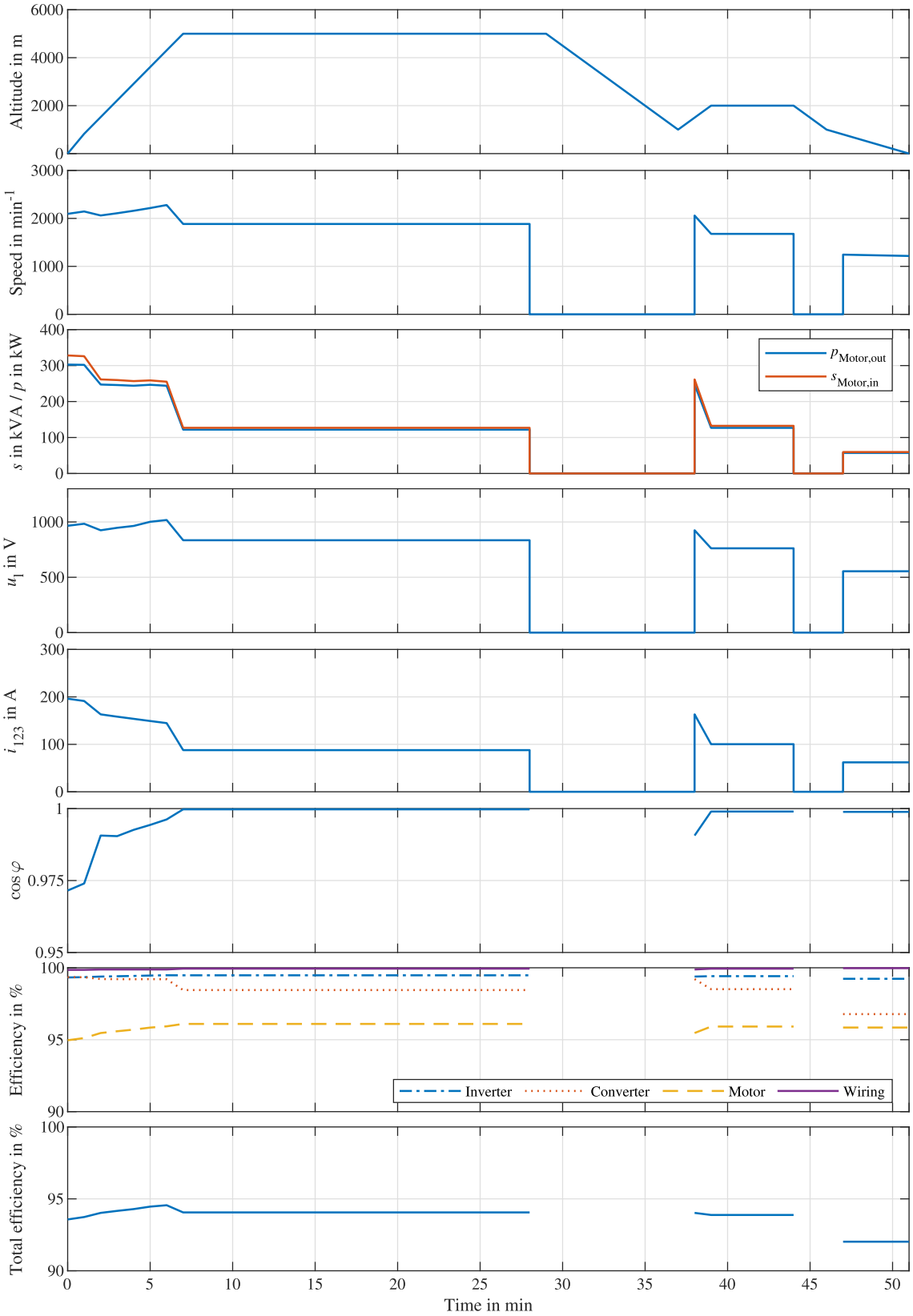

FIGURE 21. Resulting mission profile including the reserve mission for one drive unit of the final design: battery B1, motor M1, DC-link voltage $U_{\mathrm{DC}} = 2100$ V, ANPC inverter with SC-PWM and a switching frequency of $f_{\mathrm{sw,Inv}} = 30$ kHz, converter switching frequency $f_{\mathrm{sw,DAB}} = 20$ kHz. During descend, the power is reduced to zero. The propeller blade pitch is changed to rotate the blades parallel to the airflow, which stops their rotation and reduces drag. Because electric motors are used, the revelations of the propellers can be changed quickly enough to enable high dynamic adjustments.

factor close to 1 and high efficiencies of more than 95 % throughout the whole mission. This shows, considering the whole system, the benefits of a lower current density and therefore a lower utilization of the electromagnetic circuit. Finally, the partial load efficiency of the system during cruise is $\approx$ 94 %, the lowest efficiency during approach from low altitudes is $\approx$ 92 %.

For interpretation of the optimization results, the weight of the fully electric drive train is compared to the conventional propulsion system of the reference aircraft, consisting of fuel, two turboprop engines, and the propellers. The maximum fuel payload of the Beechcraft King Air 200 is given as roughly 1600 kg [14]. The weight of the empty fuel tanks is estimated as 100 kg. The two turboprop engines (P&A PT6A-42) have a mass of 190 kg per engine, the propeller mass is 55 kg each [20]. In total, the conventional propulsion system has a mass of roughly 2200 kg. The fully electric drive train has a weight of 1956 kg including propellers, which is lower than the conventional system, while the range is massively reduced to allow for the electrification of the propulsion system in the first place. Also, the weight of the conventional propulsion system is reduced during the flight mission, as the fuel is consumed. Based on this, a recalculation of the thrust requirements as shown in Equation 1 is not necessary, as the mass is practically unchanged. Also, the estimated lift-to-drag ratio can remain unchanged for the simplified calculations presented in this publication.

X. SUMMARY

In this paper, the electric power distribution and propulsion system for a short-distance commuter aircraft was investigated. The mission profile for the case study was determined in Section II. It consists of three segments (climb, cruise and descent) and takes a reserve mission into account. The power demand based on the FAA airworthiness standard for normal category aircraft and the energy demand of the aircraft were calculated in Section III. In the same section, different variants for the supply grid structure were discussed. Due to its superior potential for post-fault performance, the ''fully interconnected'' architecture was chosen for the aircraft. In Section IV, the design of the propeller and the motor was described. The information about propellers was gained from a fitting of real propeller data provided by EASA. These data were used to specify the installation space for the electric motors and to obtain realistic behavior concerning torque and rotational speed. With this information, three different categories of electric motor were designed, each with different combinations of current density, conductor material and magnet mass, which in turn were subjected to more detailed parameter variation. The parameter variation aimed to reveal the best possible combination of power density and efficiency within the three categories. The motor categories were applied to the power electronics and overall system design. The power electronic systems were discussed in Section V, including the selection of the power semiconductors and the design of the inverter and the converter realized as a DAB. The optimization included four inverter topologies (two-level, three-level T-type, NPC and ANPC inverters) and various inverter and converter switching frequencies. After this, different technologies for the wiring harness and batteries were discussed in Sections VI and VII. Finally, the safety considerations on system level were discussed in Section VIII. Protection components such as circuit breakers, RCD, and fuses to ensure the systems fault-tolerance are introduced. A quantitative system reliability analysis of different propulsion architectures is conducted to meet certification requirement, however the reliability data for the next 20 years is still with great uncertainty.

In Section IX, the optimization of the overall system is presented. For the selected design, the total mass is 1956 kg including the propellers. This is in the same range as the combined weight of fuel and engines for the reference aircraft, showing the overall feasibility of the design. Because the weight of the battery is dominating by far, all consequent components need to be designed towards maximum efficiency. By that, the total weight of the supply grid and propulsion system can be minimized.

XI. DISCUSSION

In this publication, an exemplary design of a short-range commuter aircraft was performed to gain insight into the components and parameters dominating the overall weight of the system. In the following, the outcomes and areas which need further research are discussed. For all components, usually a trade-off between high power density and high efficiency exists. Especially for the motors, a high power density seems not to be promising, as the lower efficiency and power factor are resulting in increased weight from the inverter, cabling, DC/DC-converter, and battery. This compromise can only be resolved by applying superconducting motors. By that, a high power density of the motor can be realized while also achieving a high efficiency. For example, an electromagnetic design presented in [90] can reach a gravimetric power density of 36.6 kW kg^{-1} and an efficiency of 99.88% according to analytical calculations. If these numbers can be realized with feasible effort, needs to be determined by working prototypes. Also, the effort for integrating superconductive subsystems including the auxiliary equipment, and the high technical challenges like thermal isolation are presumably too high to be feasible for smaller aircraft. While superconducting machines are worth in-depth investigation, they are mainly feasible for large passenger aircraft with very high power demands in excess of 10 MW. For smaller aircraft, a motor design like shown in this publication with focus on lower current density and therefore high efficiency is to be preferred.

The inverter topology only has minor influence on the total weight of the system. This gives room for the topology selection based on reliability and safety concerns. Multilevel inverter are generally beneficial because of the reduced voltage stress per semiconductor device. This increases the reliability of the power semiconductors under the influence

of cosmic radiation. While this was neglected in this publication because of the lower flight altitude, the failure rate due to cosmic radiation is exponentially increased for higher altitudes. For typical long-range travel altitudes of 12 km, this can require a voltage derating of the power semiconductors of more than 50%. This again strongly suggests the application of multi-level inverter. By that, also the voltage slew rates at the output are limited, which in turn reduces insulation stress at the motor. Additionally, special fault-tolerant operation schemes can be applied. Important research topics are therefore reliability and fault tolerance of inverter [48]. The tight integration of inverter and motor as assumed here is an important measure for minimizing or fully neglecting output filter requirements.

The variation of the supply grid voltage influences the weight of the wiring harness. As this weight is small compared to the batteries, reliability concerns can be pursued. Generally speaking, a higher voltage increases the voltage stress in the wiring insulation and requires the application of power semiconductors with a higher blocking voltage. Under the environmental constraints in aircraft like reduced air pressure, high effort is necessary to ensure isolation of high voltages. Even considering the full system, the influence of the voltage variation during the system optimization is minor. The voltage should therefore be selected based on reliability and safety concerns, and the minimum required motor voltage. For realistic combinations of parallel and series motor windings, a minimum DC voltage of 1 kV is expected for supply grids of future all-electric aircraft. This is also connected to the voltage of the battery modules. This voltage should also be high enough to enable fast charging to prevent long down-times of the aircraft.

For the supply grid topology, the ''fully interconnected'' topology like shown in this publication shows high post-fault performance. This can be utilized by further optimizing every component to reduce the oversizing and therefore decreasing the weight of the system, but this requires more detailed knowledge of the respective failure rates of the components. The ''single'' topology can also be beneficial. If a low supply grid voltage (for example 1 kV as stated before) and the same battery module voltage are chosen in the design process, the DC/DC converters can be omitted, reducing the weight and also increasing the reliability due to an overall less complex system. More research is necessary regarding the co-optimization of supply grid structures, reliability, and weight reduction.

The highest impact on the total weight comes from the battery. While all other subsystems already show feasible power densities even with current technology, extensive research is still needed for batteries to guarantee high enough energy and power densities. It is noted that especially for short commuter flights, which are more promising for commercialisation in the near future, an emphasize needs to be put on power density opposed to the energy density. Here, Li-ion batteries can be a feasible technology, while also giving a higher technology maturity compared to Li-Metal types. If even higher power densities compared to currently available Li-ion batteries can be realized, the overall weight can be drastically reduced. Also, the integration of the batteries in the wing structure under consideration of safety requirements needs to be further discussed and evaluated. To also enable longer flight missions, a strong increase in energy density of batteries would be necessary. For example, to realize a mission with a ground distance of 1000 km, the total output energy requirement would be 960 kW h in accordance with the mission profile used in this publication. If the same weight of the battery has to be guaranteed as determined above to not further decrease the usable carrying capacity of the aircraft, batteries with an energy density of more than 700 kW h kg^{-1} would be necessary considering the same efficiencies as determined above. This is even in excess of current estimations for future Li-Metal batteries. Enabling all-electric long-distance air travel can possibly enabled by combining batteries for peak power demand with fuel cells for high energy storage. For this, especially the storage of hydrogen needs to be further evaluated. Regarding battery modules, feasible battery voltage levels needs to be determined in conjunction with DC/DC converter topologies and voltage requirements from the motor. Other remaining challenges are fast-charging technology to guarantee short turnaround times at airports and the sustainable availability of raw materials for the batteries and the electric motor.

ACKNOWLEDGMENT

(Janine Ebersberger, Leon Fauth, Ralf Keuter, Yongtao Cao, and Yannik Freund contributed equally to this work.)

REFERENCES

[1] Our World in Data. (Jul. 27, 2022). *Cars, Planes, Trains: Where do CO_2 Emissions From Transport Come From?*. [Online]. Available: https://ourworldindata.org/co2-emissions-from-transport

[2] S. Kelly and D. K. Kumar. *Jet Fuel Costs Could Rise From New Rules to Improve Air Quality*. Accessed: Jul. 26, 2022. [Online]. Available: https://www.reuters.com/article/us-shipping-imo-jet-fuel-idUSKCN1TB2HL

[3] H. Schefer, L. Fauth, T. H. Kopp, R. Mallwitz, J. Friebe, and M. Kurrat, ''Discussion on electric power supply systems for all electric aircraft,'' *IEEE Access*, vol. 8, pp. 84188–84216, 2020.

[4] Mabanaft. *Jet A-1 Data Sheet*. [Online]. Available: https://www.mabanaft.co.uk/products/jet-a-1

[5] H.-J. Steiner, P. C. Vratny, C. Gologan, K. Wieczorek, A. T. Isikveren, and M. Hornung, ''Optimum number of engines for transport aircraft employing electrically powered distributed propulsion,'' *CEAS Aeronaut. J.*, vol. 5, no. 2, pp. 157–170, Jun. 2014.

[6] F. Orefice, F. Nicolosi, P. D. Vecchia, and D. Ciliberti, ''Aircraft conceptual design of commuter aircraft including distributed electric propulsion,'' in *Proc. AIAA Aviation Forum*, p. 4, Art. no. 06152020.

[7] M. Kruger and A. Uranga, ''The feasibility of electric propulsion for commuter aircraft,'' in *Proc. AIAA Scitech Forum*, Orlando, FL, USA, p. 10, Art. no. 01062020.

[8] J. Kammermann, I. Bolvashenkov, K. Tran, H.-G. Herzog, and I. Frenkel, ''Feasibility study for a full-electric aircraft considering weight, volume, and reliability requirements,'' in *Proc. Int. Conf. Electrotechnical Complexes Syst. (ICOECS)*, Oct. 2020, pp. 1–6.

[9] K. Kovalev, J. Nekrasova, N. Ivanov, and S. Zhurzvlev, ''Design of all-superconducting electrical motor for full electric aircraft,'' in *Proc. Int. Conf. Electrotechnical Complexes Syst. (ICOECS)*, Oct. 2019, pp. 1–5.

[10] S. Tedeschini, S. Mohamadian, and C. Cecati, ''A multi-phase multilevel powertrain for full electric aircraft,'' in *Proc. 47th Annu. Conf. IEEE Ind. Electron. Soc. (IECON)*, Oct. 2021, pp. 1–6.

[11] V. Patel, C. Buccella, and C. Cecati, "Analysis and implementation of multilevel inverter for full electric aircraft drives," *Energies*, vol. 13, no. 22, p. 6126, Nov. 2020. [Online]. Available: https://www.mdpi.com/1996-1073/13/22/6126

[12] J. P. Barnes, "Principles of high-efficiency electric flight," in *Proc. 52nd AIAA/SAE/ASEE Joint Propuls. Conf.*, Salt Lake City, UT, USA, Art. no. 07252016.

[13] P. C. Vratny, H. Kuhn, and M. Hornung, "Influences of voltage variations on electric power architectures for hybrid electric aircraft," *CEAS Aeronaut. J.*, vol. 8, no. 1, pp. 31–43, Mar. 2017.

[14] *Beechcraft. King Air B200 Specifications*. Accessed: May 15, 2022. [Online]. Available: https://web.archive.org/web/20120730075751/http://www.beechcraft.de/King-Air-B200.362+B6Jkw9MA__.0.html

[15] J. Wensveen, G. Atanasov, F. Peter, and T. Zill, "Electric commuter transport concept enabled by combustion engine range extender," presented at the Deutscher Luft-und Raumfahrtkongress, Darmstadt, Germany, 2019.

[16] R. Martinez-Val, E. Perez, and J. Palacin. *Historical Perspective of Air Transport Productivity and Efficiency*. [Online]. Available: https://arc.aiaa.org/doi/abs/10.2514/6.2005-121

[17] D. Scholz. *Aircraft Design*. Accessed: Jun. 18, 2022. [Online]. Available: https://www.fzt.haw-hamburg.de/pers/Scholz/HOOU/enhanced/index.html

[18] W. J. G. Bräunling, *Flugzeugtriebwerke: Grundlagen, Aero-Thermodynamik, Ideale Und Reale Kreisprozesse, Thermische Turbomaschinen, Komponenten, Emissionen Und Systeme* (VDI-Buch), 4th ed. Berlin: Springer-Vieweg, 2015. [Online]. Available: http://gbv.eblib.com/patron/FullRecord.aspx?p=2096699

[19] Federal Aviation Administration. § *23.2120: Climb Requirements*. Accessed: Jul. 1, 2022. [Online]. Available: https://www.law.cornell.edu/cfr/text/14/23.2120

[20] European Union Aviation Safety Agency. *Website*. Accessed: Jun. 5, 2022. [Online]. Available: https://www.easa.europa.eu/document-library/type-certificates

[21] C. N. Adkins and R. H. Liebeck, "Design of optimum propellers," *J. Propuls. Power*, vol. 10, no. 5, pp. 676–682, Sep. 1994.

[22] M. Henke, G. Narjes, J. Hoffmann, C. Wohlers, S. Urbanek, C. Heister, J. Steinbrink, W.-R. Canders, and B. Ponick, "Challenges and opportunities of very light high-performance electric drives for aviation," *Energies*, vol. 11, no. 2, p. 344, Feb. 2018.

[23] C. M. Wohlers, *Permanenterregte Synchronmaschinen Hoher Drehmomentdichte* (Berichte aus dem IAL). Garbsen, Germany: Tewiss, 2021, p. 4.

[24] Y. Zhongming and W. Bin, "A review on induction motor online fault diagnosis," in *Proc. 3rd Int. Power Electron. Motion Control Conf. (IPEMC)*, 2000, pp. 1353–1358.

[25] Y. Chen, S. Liang, W. Li, H. Liang, and C. Wang, "Faults and diagnosis methods of permanent magnet synchronous motors: A review," *Appl. Sci.*, vol. 9, no. 10, p. 2116, May 2019.

[26] M. Borghei and M. Ghassemi, "Insulation materials and systems for more- and all-electric aircraft: A review identifying challenges and future research needs," *IEEE Trans. Transport. Electrific.*, vol. 7, no. 3, pp. 1930–1953, Sep. 2021.

[27] A. Merkert, T. Krone, and A. Mertens, "Characterization and scalable modeling of power semiconductors for optimized design of traction inverters with Si- and SiC-devices," *IEEE Trans. Power Electron.*, vol. 29, no. 5, pp. 2238–2245, May 2014.

[28] D. Han, J. Noppakunkajorn, and B. Sarlioglu, "Comprehensive efficiency, weight, and volume comparison of SiC- and Si-based bidirectional DC–DC converters for hybrid electric vehicles," *IEEE Trans. Veh. Technol.*, vol. 63, no. 7, pp. 3001–3010, Sep. 2014.

[29] T. Sakaguchi, M. Aketa, T. Nakamura, M. Nakanishi, and M. Rahimo, "Characterization of 3.3 Kv and 6.5 Kv SiC MOSFETs," in *Proc. PCIM Europe Int. Exhib. Conf. Power Electron., Intell. Motion, Renew. Energy Energy Manag.*, 2017, pp. 1–5.

[30] S. Sabri, E. Van Brunt, A. Barkley, B. Hull, M. O'Loughlin, A. Burk, S. Allen, and J. Palmour, "New generation 6.5 Kv SiC power MOSFET," in *Proc. IEEE 5th Workshop Wide Bandgap Power Devices Appl. (WiPDA)*, Oct. 2017, pp. 246–250.

[31] K. Kawahara, S. Hino, K. Sadamatsu, Y. Nakao, Y. Yamashiro, Y. Yamamoto, T. Iwamatsu, S. Nakata, S. Tomohisa, and S. Yamakawa, "6.5 Kv Schottky-barrier-diode-embedded SiC-MOSFET for compact full-unipolar module," in *Proc. 29th Int. Symp. Power Semiconductor Devices IC's (ISPSD)*, May 2017, pp. 41–44.

[32] J. Ebersberger, M. Hagedorn, M. Lorenz, and A. Mertens, "Potentials and comparison of inverter topologies for future all-electric aircraft propulsion," *IEEE J. Emerg. Sel. Topics Power Electron.*, vol. 10, no. 5, pp. 5264–5279, Oct. 2022.

[33] F. Umbach, P. Brandt, S. Mansueto, W. Rusche, A. Korzenietz, D. Cassese, and U. Queitsch, "2.3 Kv—A new voltage class for Si IGBT and Si FWD," in *Proc. Int. Exhib. Conf. Power Electron., Intell. Motion, Renew. Energy Energy Manag.*, Jul. 2020, pp. 1–7. [Online]. Available: http://ieeexplore.ieee.org/xpl/mostRecentIssue.jsp?punumber=9177968

[34] D. Barater, C. Concari, G. Buticchi, E. Gurpinar, D. De, and A. Castellazzi, "Performance evaluation of a three-level ANPC photovoltaic grid-connected inverter with 650-V SiC devices and optimized PWM," *IEEE Trans. Ind. Appl.*, vol. 52, no. 3, pp. 2475–2485, May/Jun. 2016.

[35] D. Floricau, E. Floricau, and M. Dumitrescu, "Natural doubling of the apparent switching frequency using three-level ANPC converter," in *Proc. Int. School Nonsinusoidal Currents Compensation*, Jun. 2008, pp. 1–6.

[36] R. Abebe, G. Vakil, G. L. Calzo, T. Cox, S. Lambert, M. Johnson, C. Gerada, and B. Mecrow, "Integrated motor drives: State of the art and future trends," *IET Electr. Power Appl.*, vol. 10, no. 8, pp. 757–771, 2016.

[37] W. Lee, S. Li, D. Han, B. Sarlioglu, T. A. Minav, and M. Pietola, "A review of integrated motor drive and wide-bandgap power electronics for high-performance electro-hydrostatic actuators," *IEEE Trans. Transport. Electrific.*, vol. 4, no. 3, pp. 684–693, Sep. 2018.

[38] J. W. Kolar and S. D. Round, "Analytical calculation of the RMS current stress on the DC-link capacitor of voltage-PWM converter systems," *IEE Proc., Electr. Power Appl.*, vol. 153, no. 4, p. 535, 2006, doi: 10.1049/ip-epa:20050458.

[39] M. Forouzesh, Y. P. Siwakoti, S. A. Gorji, F. Blaabjerg, and B. Lehman, "Step-up DC–DC converters: A comprehensive review of voltage-boosting techniques, topologies, and applications," *IEEE Trans. Power Electron.*, vol. 32, no. 12, pp. 9143–9178, Mar. 2017.

[40] F. Krismer and J. W. Kolar, "Closed form solution for minimum conduction loss modulation of DAB converters," *IEEE Trans. Power Electron.*, vol. 27, no. 1, pp. 174–188, Jan. 2012.

[41] F. Krismer and J. W. Kolar, "Accurate power loss model derivation of a high-current dual active bridge converter for an automotive application," *IEEE Trans. Ind. Electron.*, vol. 57, no. 3, pp. 881–891, Mar. 2010.

[42] Y. H. Abraham, H. Wen, W. Xiao, and V. Khadkikar, "Estimating power losses in dual active bridge DC–DC converter," in *Proc. 2nd Int. Conf. Electric Power Energy Convers. Syst. (EPECS)*, Nov. 2011, pp. 1–5.

[43] I. Villar. *Multiphysical Characterization of Medium-Frequency Power Electronic Transformers*. Accessed: Jun. 12, 2022. [Online]. Available: https://infoscience.epfl.ch/record/143044

[44] Metglas. (Jul. 2022). *Magnetic Materials METGLAS 2605SA1 & 2605HB1M Alloy*. [Online]. Available: https://metglas.com/magnetic-materials/

[45] J. Wang and X. Jiang, "Review and analysis of SiC MOSFETs' ruggedness and reliability," *IET Power Electron.*, vol. 13, no. 3, pp. 445–455, 2020.

[46] N. Kaminski, "Reliability challenges for SiC power devices in systems and the impact on reliability testing," *Mater. Sci. Forum*, vol. 924, pp. 805–810, Jun. 2018.

[47] H. S.-H. Chung, H. Wang, F. Blaabjerg, and M. Pecht, *Reliability of Power Electronic Converter Systems*. Stevenage, U.K.: Institution of Engineering and Technology, 2015.

[48] Y. Cao, L. Fauth, A. Mertens, and J. Friebe, "Comparison and analysis of multi-state reliability of fault-tolerant inverter topologies for the electric aircraft propulsion system," in *Proc. 24th Int. Conf. Electr. Mach. Syst. (ICEMS)*, Oct. 2021, pp. 766–771.

[49] J. Colmenares, T. Foulkes, C. Barth, T. Modeert, and R. C. N. Pilawa-Podgurski, "Experimental characterization of enhancement mode gallium-nitride power field-effect transistors at cryogenic temperatures," in *Proc. IEEE 4th Workshop Wide Bandgap Power Devices Appl. (WiPDA)*, Nov. 2016, pp. 129–134.

[50] *As50881G: Wiring Aerospace Vehicle*, SAE Int., Warrendale, PA, USA, Aug. 2019.

[51] F. Dricot and H. J. Reher, "Survey of arc tracking on aerospace cables and wires," *IEEE Trans. Dielectr. Electr. Insul.*, vol. 1, no. 5, pp. 896–903, Oct. 1994.

[52] J.-R. Riba, Á. Gómez-Pau, M. Moreno-Eguilaz, and S. Bogarra, "Arc tracking control in insulation systems for aeronautic applications: Challenges, opportunities, and research needs," *Sensors*, vol. 20, no. 6, p. 1654, Mar. 2020.

[53] S. Raetzke and J. Kindersberger, "Role of interphase on the resistance to high-voltage arcing, on tracking and erosion of silicone/SiO_2 nanocomposites," *IEEE Trans. Dielectr. Electr. Insul.*, vol. 17, no. 2, pp. 607–614, Apr. 2010.
[54] T. André, F. Valensi, P. Teulet, Y. Cressault, T. Zink, and R. Caussé, "Arc tracking energy balance for copper and aluminum aeronautic cables," *J. Phys., Conf.*, vol. 825, Apr. 2017, Art. no. 012001.
[55] VDM Metals. *Data Sheet: Cuponal*. Accessed: May 25, 2022. [Online]. Available: https://www.vdm-metals.com/fileadmin/user_upload/Downloads/Brochures/Cuponal_VDM_Metals_EN.PDF
[56] Nexans. *Complete, reliable Cables Range for Aircraft*. [Online]. Available: https://www.nexans.fr/France/2011/BD_NEXANS_catal_aircraft_EN.pdf
[57] Tyco Electronics. *Aircraft Electrical Wire: Wire Manufacturers Perspective*. [Online]. Available: https://www.mitrecaasd.org/atsrac/FAA_PI-Engineer_Workshop/2001/aircraft_electrical_wire.pdf
[58] Raytronics AG. *Data Sheet: Spec 55 High Performance Wire and Cable With Etfe Coat*. [Online]. Available: https://raytronics.ch/phocadownloadpap/Datasheets/wire_and_cable/SPEC%2055%20High%20Performance%20Wire%20and%20Cable%20with%20ETFE%20coat%20Raytronics%20AG.pdf
[59] Cleantechnica. *Tesla Model 3 Battery Pack & Battery Cell Teardown Highlights Performance Improvements*. Accessed: Jul. 15, 2022. [Online]. Available: https://cleantechnica.com/2019/01/28/tesla-model-3-battery-pack-cell-teardown-highlights-performance-improvements/
[60] J. Liu, Z. Bao, Y. Cui, E. J. Dufek, J. B. Goodenough, P. Khalifah, Q. Li, B. Y. Liaw, P. Liu, A. Manthiram, Y. S. Meng, V. R. Subramanian, M. F. Toney, V. V. Viswanathan, M. S. Whittingham, J. Xiao, W. Xu, J. Yang, X.-Q. Yang, and J.-G. Zhang, "Pathways for practical high-energy long-cycling lithium metal batteries," *Nature Energy*, vol. 4, no. 3, pp. 180–186, 2019.
[61] R. Wang, W. Cui, F. Chu, and F. Wu, "Lithium metal anodes: Present and future," *J. Energy Chem.*, vol. 48, pp. 145–159, Sep. 2020.
[62] B. D. McCloskey, "Attainable gravimetric and volumetric energy density of Li-S and Li ion battery cells with solid separator-protected Li metal anodes," *J. Phys. Chem. Lett.*, vol. 6, no. 22, pp. 4581–4588, 2015.
[63] W. Xue, L. Miao, L. Qie, C. Wang, S. Li, J. Wang, and J. Li, "Gravimetric and volumetric energy densities of lithium-sulfur batteries," *Current Opinion Electrochemistry*, vol. 6, no. 1, pp. 92–99, Dec. 2017.
[64] OXIS Energy. (Apr. 2019). *Data Sheet: Ultra Light Lithium Sulfur Pouch Cell*. [Online]. Available: https://45uevg34gwlltnbsf2plyua1-wpengine.netdna-ssl.com/wp-content/uploads/2019/07/OXIS-Li-S-Ultra-Light-Cell-spec-sheet-v4.2.pdf
[65] A. F. Hofmann, D. N. Fronczek, and W. G. Bessler, "Mechanistic modeling of polysulfide shuttle and capacity loss in lithium–sulfur batteries," *J. Power Sources*, vol. 259, pp. 300–310, Aug. 2014.
[66] A. Fotouhi, D. Auger, L. O'Neill, T. Cleaver, and S. Walus, "Lithium-sulfur battery technology readiness and applications—A review," *Energies*, vol. 10, no. 12, p. 1937, Nov. 2017.
[67] P. Chen, Z. Wu, T. Guo, Y. Zhou, M. Liu, X. Xia, J. Sun, L. Lu, X. Ouyang, X. Wang, Y. Fu, and J. Zhu, "Strong chemical interaction between lithium polysulfides and flame-retardant polyphosphazene for lithium–sulfur batteries with enhanced safety and electrochemical performance," *Adv. Mater.*, vol. 33, no. 9, Mar. 2021, Art. no. 2007549.
[68] M. Kaliaperumal, M. S. Dharanendrakumar, S. Prasanna, K. V. Abhishek, R. K. Chidambaram, S. Adams, K. Zaghib, and M. V. Reddy, "Cause and mitigation of lithium-ion battery failure—A review," *Materials*, vol. 14, no. 19, p. 5676, Sep. 2021.
[69] S. Matsuda, M. Ono, S. Yamaguchi, and K. Uosaki, "Criteria for evaluating lithium–air batteries in academia to correctly predict their practical performance in industry," *Mater. Horizons*, vol. 9, no. 3, pp. 856–863, 2022.
[70] S. Ma, M. Jiang, P. Tao, C. Song, J. Wu, J. Wang, T. Deng, and W. Shang, "Temperature effect and thermal impact in lithium-ion batteries: A review," *Prog. Natural Sci., Mater. Int.*, vol. 28, no. 6, pp. 653–666, 2018.
[71] Y. Chen, L. Song, and J. W. Evans, "Modeling studies on battery thermal behaviour, thermal runaway, thermal management, and energy efficiency," in *Proc. 31st Intersociety Energy Convers. Eng. Conf. (IECEC)*, 1996, pp. 1465–1470.
[72] M. Hartmann and J. Kelly, "Thermal runaway prevention of Li-ion batteries by novel thermal management system," in *Proc. IEEE Transp. Electrific. Conf. Expo. (ITEC)*, Jun. 2018, pp. 477–481.
[73] X. Chen, X. Zhang, H. Wang, J. Jia, S. Xie, M. Zhi, J. Fu, and Q. Sun, "Influence of ambient pressure and heating power on the thermal runaway features of lithium-ion battery," *J. Electrochemical Energy Convers. Storage*, vol. 18, no. 2, p. 457, May 2021.
[74] B. V. Ratnakumar, M. C. Smart, L. D. Whitcanack, E. D. Davies, K. B. Chin, F. Deligiannis, and S. Surampudi, "Behavior of Li-ion cells in high-intensity radiation environments," *J. Electrochemical Soc.*, vol. 152, no. 2, p. A357, 2005.
[75] J. Voelcker, "Porsche's fast-charge power play: The new, all-electric taycan will come with a mighty thirst. This charging technology will slake it," *IEEE Spectr.*, vol. 56, no. 9, pp. 30–37, Sep. 2019.
[76] D. Bosche, E.-D. Wilkening, H. Kopf, and M. Kurrat, "Hybrid DC circuit breaker feasibility study," *IEEE Trans. Compon., Packag., Manuf. Technol.*, vol. 7, no. 3, pp. 354–362, Mar. 2017.
[77] L. Xu, J. Guerrero, A. Lashab, B. Wei, N. Bazmohammadi, J. Vasquez, and A. Abusorrah, "A review of DC shipboard microgrids—Part II: Control architectures, stability analysis, and protection schemes," *IEEE Trans. Power Electron.*, vol. 37, no. 4, pp. 4105–4120, Apr. 2022.
[78] ETA. *Data Sheet: Hvr 10 High Voltage Relay*. [Online]. Available: https://global.e-t-a.com/fileadmin/user_upload/Ordnerstruktur/pdf-Data/Products/Relais/Hochvoltrelais/2_eng/D_HVR10_ENG.pdf
[79] *Circuit Breakers for Equipment (CBE)*, document IEC 60934, 2019.
[80] F. Paschen, "Ueber die zum funkenübergang in luft, Wasserstoff und kohlensäure bei verschiedenen drucken erforderliche potentialdifferenz," *Annalen der Physik*, vol. 273, no. 5, pp. 69–96, 1889.
[81] ETA. *Data Sheet: Power Circuit Breaker Type 452*. [Online]. Available: https://www.e-t-a.de/fileadmin/user_upload/Ordnerstruktur/pdf-Data/Products/Schutzschalter_Sicherungsautomaten/Leistungsschutz/1_deutsch/D_452_D.pdf
[82] Mersen. *Data Sheet: Protistor Size 72 Ar*. [Online]. Available: https://ep-de.mersen.com/sites/mersen_de/files/DS-Semiconductor-Protection-Square-Body-Fuses-Protistor-Size-72-aR-1200VDC-IEC-EN.pdf
[83] J. Wang, G. Geng, K.-L. Chen, H. Liang, and W. Xu, "Event-based non-intrusive home current measurement using sensor array," *IEEE Trans. Smart Grid*, vol. 9, no. 6, pp. 5878–5886, Nov. 2018.
[84] M. V. Bendarkar, D. Sarojini, E. Harrison, and D. N. Mavris, "Evaluation of off-nominal performance and reliability of a distributed electric propulsion aircraft during early design," in *Proc. AIAA Scitech Forum*, Jan. 2021, p. 1723.
[85] C. Courtin and R. J. Hansman, "Safety considerations in emerging electric aircraft architectures," in *Proc. Aviation Technol., Integr., Oper. Conf.*, 2018, pp. 1–17.
[86] D. Kritzinger, *Aircraft System Safety: Military and Civil Aeronautical Applications*. Sawston, U.K.: Woodhead, 2006.
[87] F. Gaspari, L. Trainelli, A. Rolando, and I. Perkon. (2017). *Concept of Modular Architecture for Hybrid Electric Propulsion of Aircraft*. [Online]. Available: https://mahepa.eu/wp-content/uploads/2017/12/D1.1-Concept-of-Modular-Architecture-fro-Hybrid-Electric-Propulsion-of-Aircraft.pdf
[88] A. Hinz, B. Aigner, R. W. De Doncker, and E. Stumpf, "DC supply structure and protection concept for (hybrid) electric CS-25 aircraft," *CEAS Aeronaut. J.*, vol. 11, no. 3, pp. 623–632, Sep. 2020.
[89] J. W. Chapman, H. Hasseeb, and S. L. Schnulo, "Thermal management system design for electrified aircraft propulsion concepts," in *Proc. AIAA Propuls. Energy Forum*, Aug. 2020, pp. 1–23.
[90] M. Corduan, M. Boll, R. Bause, M. P. Oomen, M. Filipenko, and M. Noe, "Topology comparison of superconducting AC machines for hybrid electric aircraft," *IEEE Trans. Appl. Supercond.*, vol. 30, no. 2, pp. 1–10, Mar. 2020.

JANINE EBERSBERGER (Graduate Student Member, IEEE) was born in Erlangen, Germany, in 1992. She received the B.Sc. degree in engineering and business administration and the M.Sc. degree in electrical engineering from Leibniz University Hannover, Hanover, Germany, in 2017 and 2019, respectively, where she is currently pursuing the Ph.D. degree in electrical engineering. Since 2019, she has been a Research Assistant at the Institute for Drive Systems and Power Electronics, Leibniz University Hannover. Her research interests include SiC power devices and the modeling and design of high power inverters.

LEON FAUTH (Graduate Student Member, IEEE) was born in Hannover, Germany, in 1991. He received the B.Sc. and M.Sc. degrees in electrical engineering from the Leibniz University Hannover, in 2016 and 2018, respectively. He is currently pursuing the Ph.D. degree in electrical engineering. Since 2018, he has been a Research Assistant at the Institute for Drive Systems and Power Electronics, Leibniz University Hannover. In addition, he is the CEO of Hansmann Electronic, developing ultra-compact ignitors and ballast for gas-discharge-lamps in special industrial applications. His research interests include GaN power devices, high power ultrasonic applications, and hybrid topologies.

RALF KEUTER (Graduate Student Member, IEEE) was born in Meppen, Germany, in August 1990. He received the dual bachelor's degree in engineering of technical systems and an apprenticeship as an electrician for machines and drive technology from the University of Applied Science in Osnabrück, Lingen, in 2014, and the master's degree in electrical engineering from Leibniz University, in 2018. After finishing his dual bachelor's studies, he started working as an Electrical Design Engineer on induction machines for customized machines and hoisting machinery at Franz Wölfer Elektromaschinenfabrik in Osnabrück. After finishing his master's study, he started working as a Research Associate at the Institute for Drive Systems and Power Electronics, Hannover.

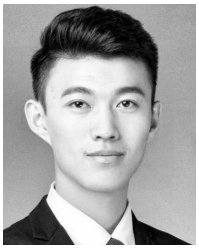

YONGTAO CAO (Graduate Student Member, IEEE) was born in Xinjiang, China, in 1992. He received the B.Eng. degree in automotive service engineering from Tongji University, in 2016, and the M.Sc. degree in electromobility from the Technische Universität Braunschweig, in 2019. He is currently pursuing the Ph.D. degree in electrical engineering with the Institute for Drive Systems and Power Electronics, Leibniz University Hannover. Since 2019, he has been a Research Assistant at the Institute for Drive Systems and Power Electronics, Leibniz University Hannover. His research interests include fault-tolerant drive system and reliability of power electronic systems.

YANNIK FREUND was born in Hanover, Germany, in 1995. He received the M.Sc. degree in engineering from Leibniz University Hannover, in 2022. He is currently pursuing the Ph.D. degree in electrical engineering. Since 2022, he has been a Research Assistant at the Institute of Electric Power Systems, Leibniz University Hannover. His research interests include electrified and hybrid aircraft propulsion system modeling and integration in aircraft design tools.

RICHARD HANKE-RAUSCHENBACH was born in Leipzig, Germany, in 1978. He received the Diploma degree in energy technology from the Hochschule für Technik, Wirtschaft und Kultur in Leipzig, in 2001, and the Ph.D. degree from the Otto-von-Guericke-Universität in Magdeburg, Germany, in 2007. Since 2014, he has been a Full Professor at Leibniz University in Hanover, Germany, where he also leads the Institute of Electric Power Systems. His lectures cover basics of electrical engineering, electrical energy storage, fuel cells, and electrolysis. His research interests include design of electrical energy storage systems, multimodal energy systems, water electrolysis, and energy system analysis.

BERND PONICK was born in Großburgwedel, Germany, in 1964. He received the Dipl.-Ing. degree in electrical power engineering from the University of Hannover, in 1990, and the Dr.-Ing. degree in electrical machines, in 1994. After nine years with Large Drives Division of Siemens as Design Engineer for large variable speed motors, the Head of electrical design, and the Technical Director at Siemens Dynamowerk Berlin. Since 2003, he has been a Full Professor of electrical machines and drive systems with the Leibniz University of Hannover. His main research interests include calculation and simulation methods for electrical machines, prediction of and measures to mitigate important parasitic effects such as magnetic noise, additional losses or bearing currents, and new applications for electrical machines, e.g., for electric and hybrid vehicles.

AXEL MERTENS (Senior Member, IEEE) received the Dipl.-Ing. and Dr.-Ing. (Ph.D.) degrees from RWTH Aachen, Germany, in 1987 and 1992, respectively.

In 1989, he was a Visiting Scholar at the University of Wisconsin at Madison. From 1993 to 2004, he was with Siemens AG in Erlangen and Nürnberg, Germany, with responsibilities for the control of large drives including a variety of converter topologies, and for a product range of medium voltage inverters. In 2004, he was appointed as a Professor of power electronics and drives at Leibniz University Hannover, Germany. He served as the Department Chair with the Department of Electrical Engineering and Computer Science and as a Spokesman of the Energy Research Center LiFE 2050, Leibniz University Hannover. In addition to his academic duties, he had responsibilities within Fraunhofer IFAM, Bremen, and Fraunhofer IEE, Kassel. He has published more than 200 scientific papers. His research interests include the application of power semiconductor devices, design of power electronic circuits and systems, and control of power converters and drives, contributing to automotive and energy applications, and industrial drives. His outstanding research contributions include applications of WBG devices in e-mobility, control and topologies of modular multilevel converters, condition monitoring of power electronic devices, and highly dynamic self-sensing control of electric machines.

Prof. Mertens has been a member of the PELS AdCom, since 2019. He served as the Chairperson of the IEEE Joint IAS/PELS/IES German Chapter. He is the Chairperson of EPE'22 ECCE Europe, Hannover. He serves as an Associate Editor for the IEEE TRANSACTIONS ON POWER ELECTRONICS.

JENS FRIEBE (Senior Member, IEEE) was born in Göttingen, Germany. He received the B.Sc., M.Sc., and Dr.-Ing. degrees in electrical engineering from the University of Kassel, Germany. He has been responsible for the research area of passive components in power electronics at the Institute for Drive Systems and Power Electronics, Leibniz University Hannover, Germany, since January 2018. Before that, he worked for more than 13 years at SMA Solar Technology, Germany, in the field of PV-inverter topologies, wide-bandgap semiconductors, magnetic components, control strategies for high switching frequencies, and power electronics packaging. He has invented more than 30 granted patents in the field of power electronics.